Localized Amplification of Seismic Waves and Correlation with Damage due to the Northridge Earthquake: Evidence for Focusing in Santa Monica

by S. Gao, H. Liu, P. M. Davis, and L. Knopoff

Abstract The analysis of seismograms from 32 aftershocks recorded by 98 seismic stations installed after the Northridge earthquake in the San Fernando Valley, the Santa Monica Mountains, and Santa Monica, California, indicates that the enhanced damage in Santa Monica is explained in the main by focusing due to a lens structure at a depth of several kilometers beneath the surface and having a finite lateral extent. The diagnosis was made from the observation of late-arriving S phases with large amplitudes, localized in the zones of large damage. The azimuths and angles of incidence of the seismic rays that give rise to the greatest focusing effects correspond to radiation that would have emerged from the lower part of the rupture surface of the mainshock. Thus the focusing and, hence, the large damage in Santa Monica were highly dependent on the location of the Northridge event, and an earthquake of similar size, located as little as one source dimension away, would not be likely to repeat this pattern. We show from coda wave analysis that the influence of surface geology as well as site effects on damage in Santa Monica is significantly smaller than are the focusing effects.

Introduction

During the 17 January 1994 $M_w = 6.7$, depth $= 19$ km Northridge earthquake (USGS and SCEC, 1994), Sherman Oaks and mid–Santa Monica experienced much greater damage than neighboring regions at similar distances from the epicenter. This is illustrated in Figure 1, which shows that the distribution of red-tagged buildings (Marshall and Stein, 1994) has higher concentrations in these areas than in the immediate surroundings. The boundary between the heavily and the slightly damaged zones is relatively sharp; the transition takes place over a distance of less than 1 km. There is no systematic difference in building types, building codes, or earthquake resistance between the heavily and the slightly damaged zones (K. Janoyan of UCLA School of Engineering, personal comm.). Thus, we concentrate our efforts at studying the causes for the large damage on the nature of the seismic wave propagation from the Northridge earthquake.

Concentrated damage patterns have been reported for the 1 October 1987 ($M_L = 5.9$) Whittier Narrows, California, earthquake; there was a strong concentration of damage along the slope of a hill 8 to 10 km from the epicenter (Kawase and Aki, 1990). The depth of the Whittier Narrows earthquake was 14 ± 1 km (Jones and Hauksson, 1988). Kawase and Aki (1990) and Aki (1993) suggest that the concentrated damage was caused by critically incident SV waves, which caused anomalous amplification on the slope of a hill on the other side of the hypocenter. As shown below,

concentrated damage in Santa Monica is unlikely to be related to this effect.

At the time of the Northridge earthquake, only one strong-motion station was located in Santa Monica (station S_MONICA) and one in Sherman Oaks (station SHR). Thus the mainshock gave insufficient information that would allow us to learn why the damage was concentrated. To understand the cause of the concentrated damage, we installed an array of seismic stations to record aftershocks in the two heavily damaged areas as well as along two profiles across the San Fernando Valley and the northwestern part of the Los Angeles Basin.

Ground motion generated by an earthquake is controlled by several factors, such as source characteristics, propagation path, surface geology, topography, and underground structure. Our objective was to evaluate the relative importance of seismic wave propagation through deeper structure, which could be evaluated using seismic waves from aftershocks and local site effects.

Experiment and Data

Between 26 March and 16 April 1994, 98 seismic stations were deployed to record aftershocks of the Northridge earthquake (Fig. 2 and Table 1). The stations were located in two clusters and along two profiles. Some stations belong to both clusters and profiles. The western profile had 20 sta-
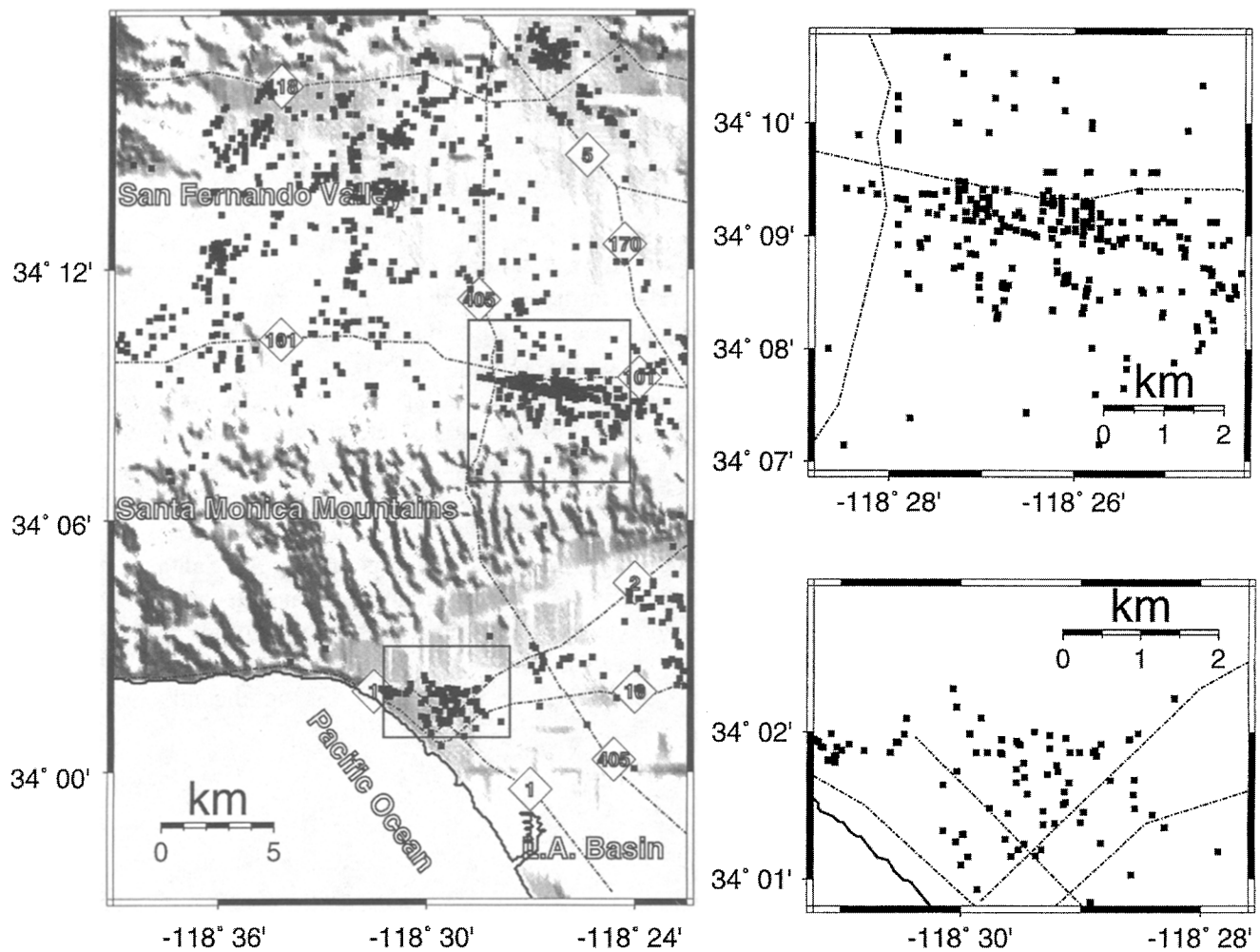
Figure 1. Distribution of red-tagged buildings and topography. The coordinates of the red-tagged buildings are from Marshall and Stein (1994). Diagrams on the right are enlargements of the inset areas.

tions, and the eastern one, 16 stations. Both profiles were about 35-km long, along lines with strike 165°, and traversed the San Fernando Valley, Santa Monica Mountains, and the northwestern part of the Los Angeles Basin. The northern cluster of 36 stations was centered in Sherman Oaks in a 7 by 7 km area; the distance and azimuth of the center of the Sherman Oaks cluster (station B16) from the epicenter are about 11 km and 133°. The southern cluster of 29 stations was centered in Santa Monica in a 4 by 3 km area; the distance and azimuth of this cluster (station F10) from the epicenter are about 21 km and 168°.

All stations were equipped with Reftek digital recorders. A trigger mode was used to record relatively strong events. The length of each seismogram was 80 sec, including 20 sec of pretriggering time. The long pretriggering time proved to be useful, because the S waves from some events were the triggering signals at some stations, and the long pretriggering time saved the first arrival. The sampling rate was set at 125 samples per second, and the data format was 16 or 32 bit, depending on the type of Reftek recorder (72A-02, 72A-06, 72A-07, or 72A-08). About half of the stations were equipped with GPS receivers and thus had relatively accurate times and locations. The clocks of stations without GPS receivers were corrected every week during station service using external GPS clocks, and the locations for those stations were obtained from USGS 1:24,000 series topographic maps.

There were 75 stations equipped with L28 4.5-Hz sensors, 8 with L22 2.0-Hz sensors, and 15 with L4C 1-Hz sensors. The amplitudes of the seismograms from the sensors were standardized to the uniform response function of an L28. There were no obvious relations between the corrected amplitude and sensor type, as shown below. The station locations and sensor types are listed in Table 1 and shown in Figure 2.

Five of the 98 stations could not be used because (1) of malfunctioning amplifiers, (2) data could not be recovered
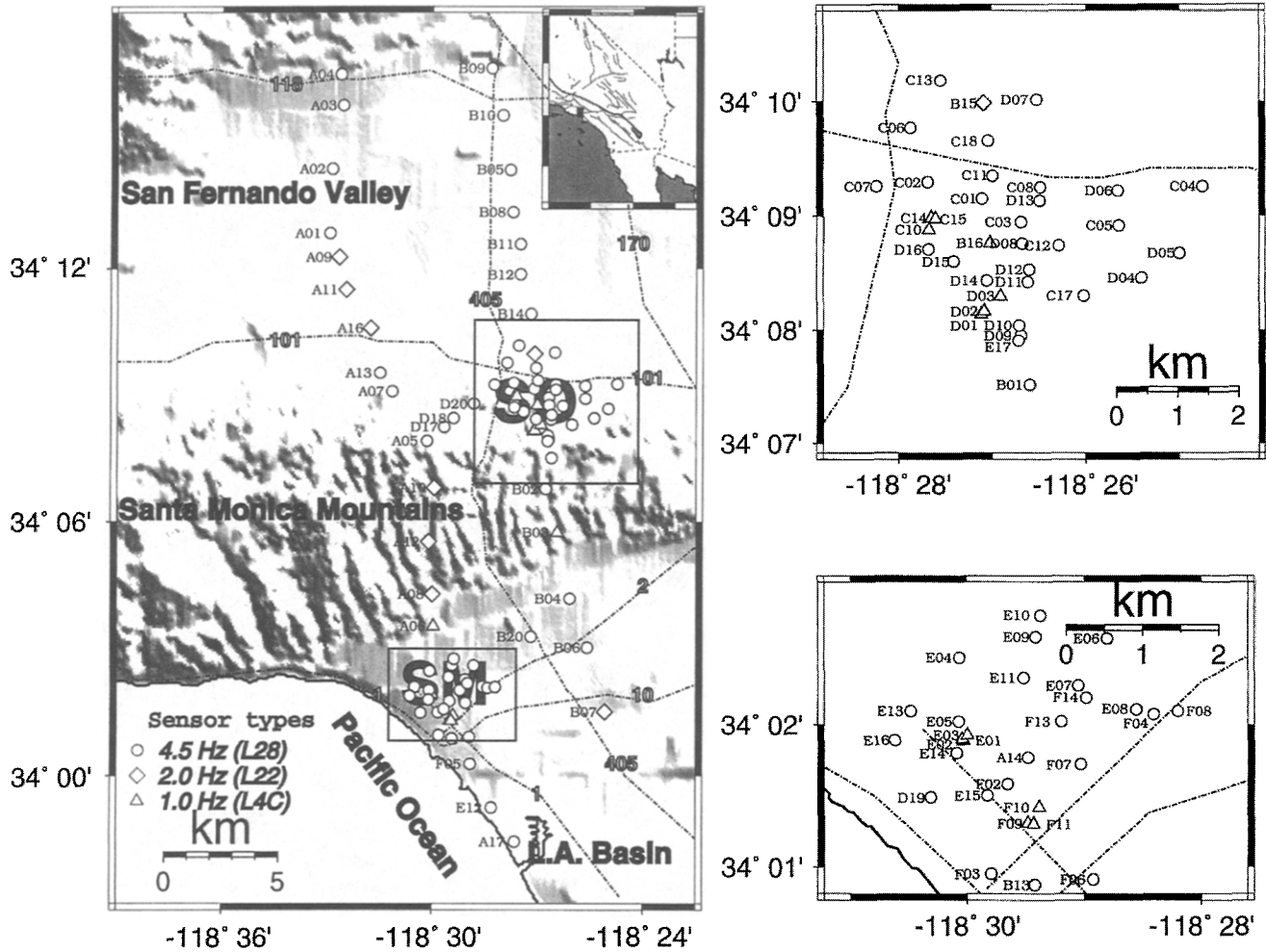
Figure 2.   Station locations, station numbers, and sensor types. Circles are 4.5-Hz (L28) sensor stations, diamonds are 2.0-Hz (L22) sensor stations, and triangles are 1-Hz (L4C) stations. The inset at the center upper right shows the location of the larger map (small black square). The Sherman Oaks (SO) and Santa Monica (SM) areas are enlarged at the right. Numbered lines are highways; highway 2 is Santa Monica Boulevard. About 7 gigabytes of data were recorded during the experiment.

from a bad disk, or (3) of failure to be triggered by any of the events we selected for this study.

We studied 32 events from among more than 1500 events that triggered at least one of the stations (Fig. 3 and Table 2). The events were selected according to the following criteria: (1) The event must have triggered at least 40 stations. (2) The event was not strong enough to clip more than 10 of the stations seriously. (3) The events chosen exhibited significant temporal separation from other strong local events; i.e., the seismograms did not overlap.

Figure 3 shows the epicenters of the 32 events. They cover the entire aftershock zone of the Northridge earthquake approximately. The triggering rate and quality of the data depend on the magnitudes and other parameters of the events, as well as ground noise, which in the cities is directly

related to local time. The triggering parameters were different from station to station in order to minimize "false" triggering, which was mostly caused by passing vehicles.

The Reftek recorder computes a running ratio of the short-time average (STA) and long-time average (LTA) of a selected seismometer component, and an event is declared when the ratio exceeds a programmed threshold, which is called the trigger ratio. Initially, we used the triggering parameters, LTA window = 15 sec, STA window = 0.2 sec, and trigger ratio = 8.0, for most of the stations. After the first week, the parameters were adjusted for some of the stations based on their performance. For stations in populated valleys and basins, a lower trigger ratio of 3.0 to 5.0 and smaller STA window of 0.1 to 0.15 sec was found to be more effective in discriminating signals in regions of high

Table 1

Stations Used in This Study and S-Wave Amplification Factors

Station Name	Coordinates		Sensor Type	Amplitudes		Standard Errors		No. of Events
	Latitude (°N)	Longitude (°E)		P wave	S wave	P wave	S wave	
A01	34.213924	−118.548698	L28	0.98	0.68	0.14	0.11	27
A02	34.238934	−118.547394	L28	0.93	0.67	0.13	0.11	32
A03	34.263672	−118.542450	L28	0.45	0.61	0.39	0.39	1
A04	34.275669	−118.543457	L28	0.72	0.89	0.12	0.13	26
A05	34.131889	−118.502686	L28	0.77	0.57	0.12	0.10	31
A06	34.058853	−118.499374	L4C	0.88	0.73	0.13	0.12	31
A07	34.151409	−118.519020	L28	1.07	1.17	0.15	0.16	26
A08	34.071354	−118.500000	L22	1.20	0.90	0.40	0.39	1
A09	34.204437	−118.544273	L22	1.30	1.19	0.17	0.16	30
A10	34.113281	−118.499084	L22	1.25	0.97	0.18	0.15	19
A11	34.191669	−118.540886	L22	1.27	1.32	0.17	0.18	31
A12	34.092056	−118.501823	L22	1.35	1.12	0.19	0.18	13
A13	34.158855	−118.524872	L28	0.78	0.58	0.12	0.10	31
A14	34.029427	−118.491402	L28	0.83	1.20	0.13	0.17	25
A16	34.176548	−118.529167	L22	0.89	0.73	0.13	0.12	28
B01	34.125263	−118.443398	L28	0.67	0.81	0.11	0.12	32
B02	34.112915	−118.446220	L28	0.94	1.02	0.16	0.16	14
B03	34.095833	−118.440758	L4C	0.64	0.95	0.12	0.15	18
B04	34.069660	−118.434639	L28	1.43	0.84	0.18	0.13	30
B05	34.238670	−118.463280	L28	1.96	0.64	0.24	0.11	31
B06	34.050522	−118.426300	L28	0.70	1.54	0.11	0.20	31
B07	34.025185	−118.417915	L22	0.90	0.96	0.15	0.15	17
B08	34.222137	−118.461845	L28	1.16	0.45	0.16	0.10	27
B10	34.259895	−118.466927	L28	1.62	0.71	0.20	0.11	31
B11	34.209637	−118.458328	L28	1.18	0.47	0.16	0.10	28
B12	34.197735	−118.458328	L28	1.21	0.57	0.16	0.10	32
B13	34.014610	−118.490417	L28	1.31	1.50	0.18	0.20	21
B14	34.182293	−118.453384	L28	1.60	1.24	0.20	0.17	30
B15	34.166416	−118.451508	L22	1.04	0.80	0.27	0.26	3
B16	34.146069	−118.450325	L4C	0.85	0.84	0.13	0.13	29
B20	34.054688	−118.453125	L28	1.93	0.67	0.33	0.25	3
C01	34.152493	−118.451706	L28	1.10	1.29	0.16	0.18	21
C02	34.154907	−118.461411	L28	0.69	0.80	0.42	0.42	1
C03	34.149090	−118.444923	L28	1.22	1.05	0.17	0.15	24
C04	34.154320	−118.412445	L28	1.55	2.39	0.46	0.51	1
C05	34.148598	−118.427498	L28	0.86	0.82	0.13	0.13	26
C06	34.162838	−118.464607	L28	0.78	0.55	0.13	0.11	21
C07	34.154297	−118.470573	L28	1.14	0.85	0.15	0.13	28
C10	34.147968	−118.461243	L4C	2.19	1.87	0.27	0.25	20
C11	34.155861	−118.449867	L28	0.99	0.81	0.14	0.13	23
C12	34.145744	−118.438126	L28	1.05	1.26	0.15	0.17	25
C13	34.169792	−118.459114	L28	0.83	0.57	0.17	0.16	8
C14	34.149746	−118.460838	L4C	2.16	1.64	0.26	0.21	32
C15	34.149471	−118.460495	L4C	2.20	2.30	0.27	0.30	20
C17	34.138355	−118.433693	L28	0.83	1.29	0.12	0.17	31
C18	34.160938	−118.450775	L28	0.95	0.70	0.14	0.12	26
D01	34.135647	−118.451981	L4C	1.07	0.85	0.15	0.14	21
D02	34.136059	−118.451416	L4C	1.26	1.68	0.17	0.22	30
D03	34.138283	−118.448410	L4C	0.89	0.85	0.13	0.13	24
D04	34.140984	−118.423386	L28	1.06	0.91	0.15	0.14	26
D05	34.144588	−118.416656	L28	1.01	1.12	0.14	0.16	31
D06	34.153667	−118.427567	L28	1.21	1.04	0.16	0.15	26
D07	34.166927	−118.442055	L28	0.93	1.01	0.14	0.15	27
D08	34.146019	−118.444664	L28	0.75	0.80	0.12	0.12	31
D09	34.132534	−118.444878	L28	1.20	1.88	0.16	0.24	28
D10	34.133999	−118.445267	L28	1.11	0.76	0.15	0.12	32
D11	34.140366	−118.443619	L28	0.48	0.28	0.31	0.30	2
D12	34.142200	−118.443428	L28	0.95	2.01	0.14	0.26	28
D13	34.152264	−118.441460	L28	1.00	0.83	0.14	0.13	27

Table 1

Continued

Station Name	Coordinates		Sensor Type	Amplitudes		Standard Errors		No. of Events
	Latitude (°N)	Longitude (°E)		P wave	S wave	P wave	S wave	
D14	34.140572	−118.450905	L28	0.96	1.50	0.22	0.26	5
D15	34.143444	−118.456841	L28	1.75	1.51	0.22	0.20	31
D16	34.145138	−118.461327	L28	1.01	0.85	0.14	0.13	30
D17	34.137371	−118.494400	L28	1.01	1.22	0.14	0.17	26
D18	34.140820	−118.489838	L28	0.74	0.41	0.11	0.09	31
D19	34.024738	−118.505211	L28	1.19	1.53	0.16	0.20	28
D20	34.146542	−118.480446	L28	0.86	0.36	0.15	0.12	14
E01	34.031418	−118.500587	L4C	1.18	2.22	0.17	0.29	21
E02	34.031605	−118.500717	L4C	0.82	2.04	0.14	0.27	15
E03	34.032093	−118.499985	L4C	0.73	1.25	0.12	0.18	22
E04	34.041210	−118.501053	L28	0.39	0.43	0.10	0.11	19
E05	34.033703	−118.501236	L28	0.58	1.03	0.10	0.15	30
E06	34.043381	−118.480064	L28	0.49	0.67	0.11	0.12	20
E07	34.037910	−118.484177	L28	0.34	0.42	0.11	0.11	17
E08	34.035156	−118.475914	L28	0.68	0.45	0.14	0.13	12
E09	34.043594	−118.490288	L28	0.28	0.25	0.28	0.28	2
E10	34.046093	−118.489578	L28	0.68	0.35	0.13	0.11	15
E11	34.038803	−118.492004	L28	0.58	0.34	0.11	0.10	22
E12	33.987370	−118.471619	L28	0.70	0.44	0.18	0.17	6
E13	34.034897	−118.508072	L28	0.70	0.65	0.14	0.14	14
E14	34.029949	−118.501564	L28	0.88	2.56	0.13	0.32	32
E15	34.025002	−118.497131	L28	1.12	1.11	0.15	0.16	26
E16	34.031467	−118.510361	L28	1.16	1.71	0.17	0.23	17
E17	34.131767	−118.445312	L28	0.65	0.41	0.11	0.09	29
F03	34.015884	−118.496613	L28	0.49	0.51	0.11	0.11	18
F04	34.034504	−118.473434	L28	0.55	0.14	0.24	0.23	3
F05	34.004688	−118.481773	L28	0.81	0.45	0.17	0.15	8
F06	34.015224	−118.482063	L28	1.20	1.39	0.22	0.23	6
F07	34.028645	−118.483849	L28	0.83	1.07	0.13	0.15	25
F08	34.034908	−118.469986	L28	0.68	1.11	0.12	0.16	22
F09	34.021729	−118.491440	L4C	1.15	1.60	0.18	0.23	12
F10	34.023560	−118.489738	L4C	1.08	1.51	0.20	0.24	7
F11	34.021648	−118.490639	L4C	1.04	1.61	0.19	0.25	8
F13	34.033722	−118.486588	L28	0.39	0.39	0.10	0.10	21

ground noise. In contrast, for stations on bedrock, a high trigger ratio of 10.0 to 15.0 and small LTA window 5.0 to 10.0 sec were effective in reducing vehicle triggers.

Figure 4 shows six raw 3-component seismograms and their spectra from event 1 at two stations 650 m apart in Santa Monica; the top set of three traces was recorded at station A14 in a zone of heavy damage and the lower set of three at station F13 in a zone of light damage. The *P*- and *S*-wave amplitudes are about four and seven times stronger, respectively, at the station in the heavily damaged zone. The ratio of *S*-wave coda amplitudes between the two stations is about 2:1, which is obviously much smaller than the ratio of the *S*-wave amplitudes.

Method and Results

We determined the maximum amplitudes of the ground velocity on the vertical sensor within a window that opened approximately 2 sec before and closed 2 sec after the first *P*-wave arrival, and the maximum amplitudes on the hori-

zontal components within a window that opened 3 sec before and closed 3 sec after the first *S* arrival. We formed the vector sum of the two horizontal component amplitudes.

The magnitudes of the events in this study range from 1.7 to 3.5. The corresponding corner frequencies are expected to be greater than 2.0 Hz (Aki and Richards, 1980), which is within the range of frequencies that we have used. However, for this initial study, we assume that the focusing effects are frequency independent, and we consider frequency dependence at a later time.

The amplitudes for both *P* and *S* waves were corrected for geometrical spreading and attenuation by assuming an isotropic and homogenous medium; i.e.,

$$A = rA' \exp \frac{\pi(r - 1)f}{cQ}, \quad (1)$$

where A' is the amplitude measured directly from the seismogram; r is the hypocentral distance; A is the equivalent, corrected amplitude at $r = 1$ km; f is the dominant fre-
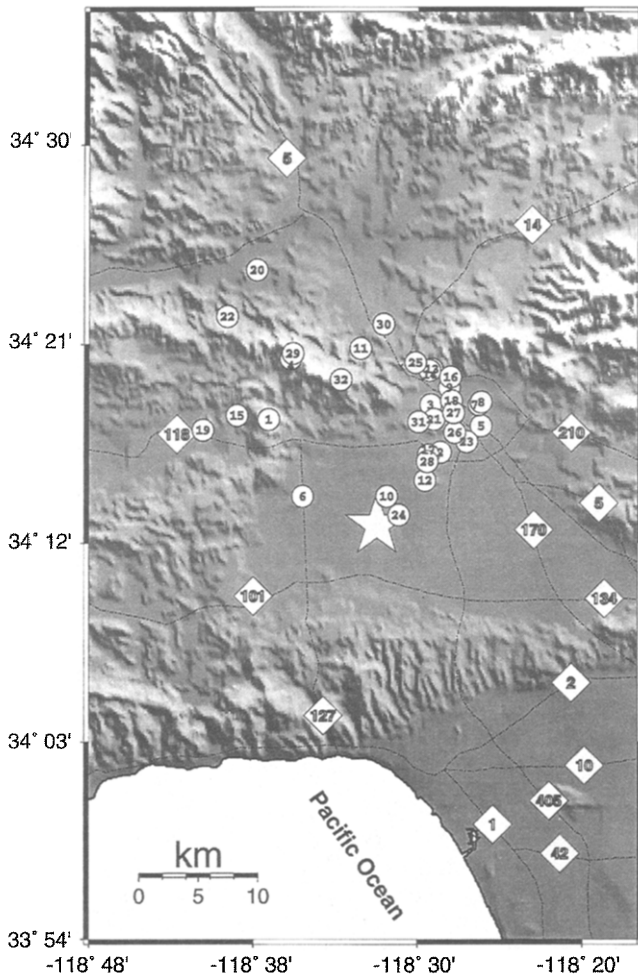
Figure 3.   Epicenters of the 32 aftershocks used in this study. Diamonds indicate major numbered highways. The epicenter of the mainshock is indicated by the star.

quency, which is 7.0 Hz for P and 4.0 Hz for S waves; c is velocity, which we take to be 5.0 km/sec for P and 3.0 km/sec for S waves; and Q is the attenuation factor, which we assume is 150 for P and 100 for S waves.

The P- or S-wave averaged amplification factors are obtained using Bayesian nonlinear inversion (Jackson and Matsu'ura, 1985). If all the events had been recorded by all the stations, the optimal amplification factors relative to the mean can be found by solving the system of equations

$$\frac{A_{ij}}{\sum_{k=1}^{I} A_{kj}} = \frac{F_i}{\sum_{k=1}^{I} F_k} \qquad (2)$$

under the constraint

$$\sum_{k=1}^{I} F_k = I, \qquad (3)$$

where A_{ij} is the corrected P- or S-wave amplitude at the ith station from the jth event, I is the total number of stations, and F_i is the optimal amplification factor for the ith station. If the total number of events is J, then $I \cdot J$ equations must be solved for the I amplification factors.

If some event-station pairs were unrecorded, the sum of amplitudes on the left side can be replaced by a weighed sum of the corresponding amplification factors. The above system of equations becomes

$$\frac{A_{ij}}{\sum_{k=1}^{N_j} A_{kj} + w_j \sum_{k=N_j+1}^{I} F_k} = \frac{F_i}{I}, \qquad (4)$$

where N_j is the number of stations that recorded the jth event and w_j is a scaling factor for the jth event.

The unknown parameters in equation (4) are the I amplification factors and the J scaling factors. In this study, $I = 93$, $J = 32$, and the total number of data points for P- or S-wave amplitudes is 1983. Therefore, the number of degrees of freedom is 1858.

We used a normalized form of equation (4) for the inversion:

$$B_{ij} = \left(N_j + W_j \sum_{k=N_j+1}^{I} F_k\right)\frac{F_i}{I}, \qquad (5)$$

where $B_{ij} = A_{ij}\,(N_j/\sum_{k=1}^{N_j} A_{kj})$ and $W_j = w_j\,(N_j/\sum_{k=1}^{N_j} A_{kj})$.

The starting parameter F_{0i} was taken to be the relative amplitude at the ith station averaged over all the events recorded by the station:

$$F_{0i} = \frac{1}{M_i}\sum_{j=1}^{M_i} B_{ij}, \qquad (6)$$

where M_i is the number of events recorded by the ith station. The standard deviation of F_{0i} is set to be 0.5. The starting value of W_j is set to be 1.0 with standard deviation of 0.5.

Empirical tests using artificial data sets indicated that the above procedure could always find the expected parameters, but the convergence was slow due to high nonlinearity. Therefore, a large number of iterations are required. The final amplification factors were obtained after 200 iterations, which takes about 12 hr on a SUN Sparc-5 workstation. The standard deviations of the parameters were computed from the covariance matrix. Figure 5 shows the starting and final values of the P- and S-wave amplification factors for all the stations as a function of the station latitudes. The starting and final values are close to each other: the difference between the starting and final amplification factors for S waves ranges from -0.08 to 0.06 with a mean of 0.001 ± 0.022, while the difference between the starting and final parameters ranges from -0.14 to 0.09 with a mean of 0.000 ± 0.035 for P waves. These differences are small because the events that were used in this study were recorded by a large number of stations (on average 67%). If all events had been

Table 2
Events Used in This Study

Event No.	Origin Day	Origin Time (UT)	Coordinates Latitute (°N)	Coordinates Longitude (°E)	Depth (km)	Mag.	No. of Stations	XCC_P	XCC_S	S ratio
1*	090	1136:18.7	34.293	−118.636	13.8	2.2	69	0.29	0.77	3.94
2	090	2027:18.6	34.268	−118.479	9.8	2.2	57	0.68	0.71	2.22
3	092	1218:41.0	34.304	−118.488	9.2	2.0	53	0.81	0.72	1.71
4*	093	0909:21.7	34.339	−118.616	12.9	2.6	77	0.78	0.84	4.03
5	093	1427:37.8	34.288	−118.442	11.1	1.7	40	0.56	0.75	—
6	093	1828:24.0	34.235	−118.605	17.9	2.7	76	0.35	0.69	5.54
7	094	0519:01.5	34.304	−118.444	7.9	2.2	65	0.43	0.72	1.59
8	094	1006:55.1	34.306	−118.442	7.7	2.2	81	0.63	0.76	2.05
9	094	1205:41.0	34.317	−118.471	7.2	1.9	51	0.58	0.69	1.90
10	095	0547:15.5	34.235	−118.528	13.6	2.0	64	0.40	0.71	6.82
11	096	0918:58.3	34.347	−118.552	4.6	2.9	79	0.42	0.69	2.31
12	096	1051:35.8	34.247	−118.493	10.2	2.0	72	0.41	0.72	2.72
13	097	0419:27.8	34.331	−118.487	5.9	3.5	78	0.40	0.74	2.05
14	097	0440:07.7	34.330	−118.489	5.7	2.6	52	0.58	0.76	2.13
15*	097	0955:31.2	34.296	−118.665	7.7	2.4	74	0.58	0.51	2.52
16	098	1345:08.1	34.325	−118.470	8.0	2.3	58	0.68	0.73	1.78
17	098	1436:21.9	34.266	−118.490	9.9	2.4	59	0.61	0.67	2.86
18	098	1715:16.9	34.307	−118.469	8.1	2.8	57	0.65	0.75	2.44
19*	099	1229:52.5	34.285	−118.696	12.1	2.5	72	0.34	0.61	3.55
20*	099	1310:10.5	34.406	−118.647	13.9	2.5	53	0.41	0.54	2.42
21	099	1515:04.2	34.293	−118.485	9.0	2.3	61	0.55	0.87	3.10
22*	099	1915:39.0	34.371	−118.674	10.2	2.8	63	0.41	0.66	2.53
23	099	2118:24.5	34.276	−118.455	10.4	2.5	69	0.66	0.58	2.62
24	100	0829:44.5	34.221	−118.517	18.0	1.7	50	0.44	0.71	—
25	100	1601:21.7	34.336	−118.502	7.1	2.6	52	0.30	0.83	2.23
26	101	0543:39.1	34.283	−118.466	10.1	1.8	55	0.55	0.51	—
27	102	0806:03.6	34.298	−118.467	7.8	1.8	49	0.57	0.59	2.26
28	102	1127:20.1	34.261	−118.491	11.8	1.8	56	0.79	0.76	2.42
29*	103	0157:31.1	34.343	−118.614	10.4	3.2	62	0.48	0.63	3.29
30	103	1118:25.1	34.365	−118.531	2.0	2.8	64	0.51	0.66	1.96
31*	103	1529:41.2	34.291	−118.499	7.3	2.6	57	0.46	0.82	2.85
32	104	0642:21.2	34.323	−118.570	3.4	2.5	58	0.40	0.58	2.70

*Events with observable secondary phases.

recorded by all stations (i.e., $M_i = J$, $N_j = I$), then $F_{0i} = F_i$. However, when some of the events were recorded by only a small number of stations, the difference could be significant.

We use cross-correlation coefficients (XCC) to quantify the coherence of the relative amplitudes from different events. The coherence of the jth event with the amplification factor pattern is computed using

$$\text{XCC}_j = \frac{\sum_{i=1}^{K} (F_i - \bar{F})(B_{ij} - \bar{B}_j)}{\sqrt{\sum_{i=1}^{K} (F_i - \bar{F})^2 \sum_{i=1}^{K} (B_{ij} - \bar{B}_j)^2}}, \quad (7)$$

where K is the number of common stations between the jth event and the amplification factor pattern, $\bar{F}$ is the averaged amplification factor for all of the events and the K stations, $\bar{B}_j$ is the averaged relative amplitude for the jth event.

The mean number of measurements for a given station is 21 ± 10. The amplification factors F_i for both P and S waves and their standard deviations computed from the co-

variance matrices are listed in Table 1 and plotted in Figures 6 and 7. The standard deviations for both P- and S-wave amplification factors is about 10% of the mean.

The final P- and S-wave amplification patterns have a cross-correlation coefficient (XCC) of 0.50. For the P-wave factors, the ratio of the largest to the smallest value is about 7; for S waves, the ratio is as large as 17. The mean XCC of the S-wave amplification pattern of an individual event and the averaged pattern for S waves is 0.69 ± 0.09; for P waves, the mean XCC is 0.53 ± 0.14 (Table 2). The S-wave pattern is more consistent from event to event than the P-wave pattern.

Discussion

Comparison with Damage Pattern. Our aftershock amplitude results (Figs. 6 and 7) show a general agreement with the distribution of red-tagged buildings shown in Figure 1. In the two heavily damaged zones of southern Sherman Oaks and mid–Santa Monica, the relative amplitudes are more and
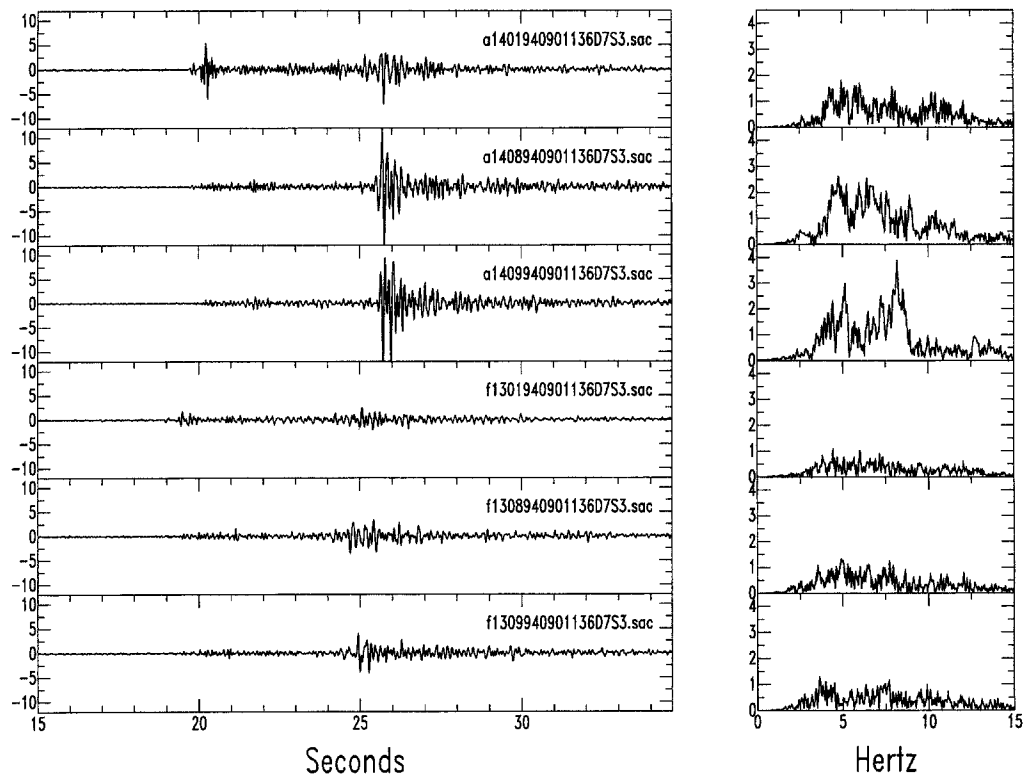
Figure 4.   Three-component sample seismograms (vertical, radial, and transverse components) and their spectra from event 1 at two stations 650 m apart. The three traces at the top are recordings from station A14 located in Santa Monica's heavily damaged zone, and the three traces at the bottom are recordings from station F13 located in the slightly damaged zone. The P- and S-wave amplitudes are about four and seven times stronger, respectively, while the ratio of S-wave coda amplitudes between the two stations is about 2:1. All traces are plotted to the same scale.

often much more than three times larger than those in neighboring areas. Figure 8 displays a smoothed version of the damage pattern together with the P- and S-wave averaged amplitudes and topography along a north–south profile. Because the boundaries between the heavily damaged and slightly damaged zones in Sherman Oaks and Santa Monica are nearly E–W, and the change from one zone to another is sudden, the number of red-tagged buildings was counted within an E–W elongated rectangle of 2 by 0.5 km and centered at the station.

In Figure 9, we display normalized P- and S-wave amplification factors and the smoothed damage patterns for Santa Monica and Sherman Oaks. Some of the features of the diagrams include the following: (1) The boundaries that separate the heavily damaged and slightly damaged zones are also boundaries that separate high- and low-amplification factors. (2) Below a threshold S-wave amplification of about 0.2 in Santa Monica (Fig. 9a) and perhaps in Sherman Oaks as well (Fig. 9c), the number of red-tagged buildings is nearly zero. (3) The correlation between the S-wave amplification factor and damage is higher than between the P-wave factor and damage pattern.

The XCC provides a quantitative estimate of the relationship between the amplification factors and damage as given by the number of red-tagged buildings. This XCC for Santa Monica is 0.59 for S waves and 0.15 for P waves; for Sherman Oaks, it is 0.06 for S waves and 0.00 for P waves. The reasons for the low XCC's may include that (1) the relation between the number of red-tagged buildings and the amplification factors may not be linear; (2) the density of buildings is not uniform; and (3) as discussed below, the amplification factors are closely related to source locations. The average of the amplification factors over all the aftershocks is different from that for the mainshock, which was responsible for the damage pattern.

In Sherman Oaks, there is a close relationship between the amplitude pattern and the topography, as shown in Figures 6 and 7. For the Sherman Oaks case, the largest amplitudes occur along the southern boundary of the valley floor and along the north slope of the Santa Monica Mountains. We interpret these observations for the Sherman Oaks area separately; at this time, there are no clear relationships that pinpoint the mechanism. We therefore concentrate our efforts on the Santa Monica data.
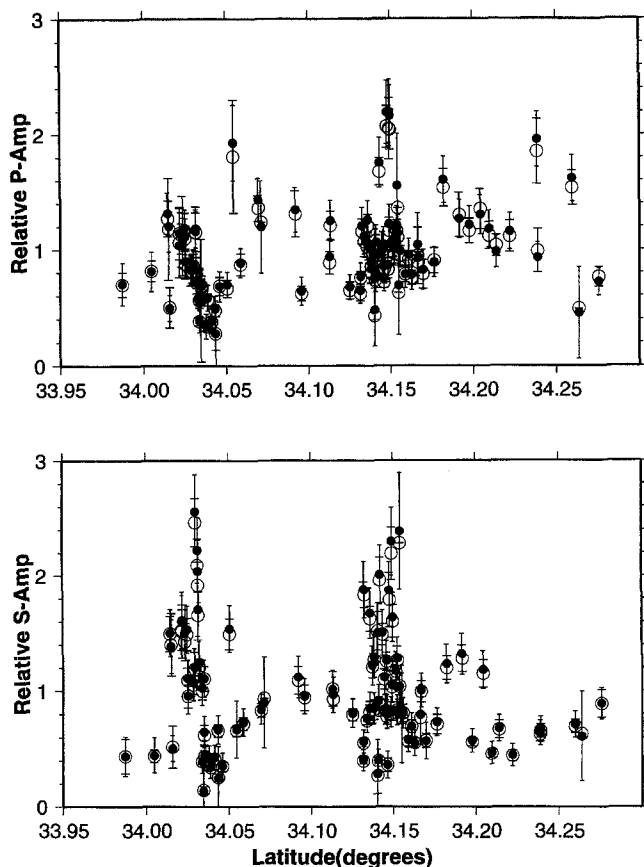
Figure 5. Starting and final amplification factors for the Bayesian inversion. The large open circles and error bars with long horizontal bars are the starting parameters and their errors, and the small filled circles and error bars with short horizontal bars are the final parameters and their errors from the inversion.

Secondary Phases in Santa Monica. A north–south seismic section for stations in Santa Monica reveals a strong secondary phase. Figure 10 shows a 3-component record section from event 1; we show the first 9 sec of the seismograms after the first *P* arrival. The traces are aligned with the first arrivals, and all are plotted using the same scale. One of the most impressive features of Figure 10a is that the strongest phase on the vertical traces is *not* the first *P* arrival but is instead a secondary phase that arrives less than 1 sec later, with a higher apparent velocity than that of the first *P* wave. The two phases converge near station F10, which is approximately at the center of the damage zone. In the heavily damaged zone (traces E02 through B13), the amplitudes of the secondary phase are about 10 times stronger than the first *P* wave and are reduced sharply at stations in the slightly damaged zone (traces E06 through E05). However, the amplitudes of the first *P* phase, where it can be identified, do not vary significantly. Event 4 displays the same anomalous amplitude for the late-arriving *P* waves (Fig. 11a).

A secondary phase can be recognized on the horizontal component seismograms for the *S* waves as well. The am-

plitude of the second *S* arrival is as much as 10 times stronger in the heavily damaged zone than at stations north and south of it (Figs. 10b, 10c, 11b, and 11c). However, the first *S* phases all have similar amplitudes whether in the high damage zone or outside it, as in the case of the *P* waves. The secondary *S* arrivals are largely *SH* waves having much larger amplitudes on the two horizontal components than on the verticals.

For the events with observable secondary phases in the area between latitudes 34.025° and 34.045°, the mean apparent velocity of the first *P* wave is about 2.5 ± 0.3 km/sec, and that of the secondary *P* wave is about 5.0 ± 0.5 km/sec. If we assume that the near-surface *P*-wave velocity in Santa Monica is 1.5 km/sec, then the angle of incidence measured from the vertical is about 38° ± 5° and 18° ± 3° for the first and secondary *P* waves, respectively. For the first and secondary *S* waves, the apparent velocities are about 1.4 ± 0.3 and 2.5 ± 0.5 km/sec, respectively; under the assumption that the near-surface *S*-wave velocity is 0.8 km/sec, the angles of incidence are 37° ± 9° and 20° ± 4° for the first and secondary *S* waves, respectively, results that are not in significant disagreement with the angles for the *P*-wave arrivals.

Aftershocks that display clear secondary phases are mostly deep and concentrated on the northwestern side of the aftershock zone (see Fig. 13 and Table 2). For these events, the ratio of the amplitudes on the horizontal component traces between the heavily damaged and slightly damaged zones is much larger than for those aftershocks that do not show the large secondary phase, thus implying that it is the large secondary phase that is responsible for the damage in mid–Santa Monica. Two exceptions are events 6 and 10, which are deep and have the largest ratios but do not have identifiable secondary phases; we discuss the geometry of these events below. The existence of the secondary phases can be well explained by the preliminary structural model proposed at the end of this section (Fig. 17).

Effects of Earthquake Location and Magnitude. To understand the role of the geometry of the source on the differential damage caused by the mainshock, we undertook a systematic study of the influence of individual aftershock sources on the amplification of the seismic signals. We divided the Santa Monica region into two subzones: the middle part that was heavily damaged during the Northridge earthquake with 17 stations and the northern part that was slightly damaged with 11 stations.

For each of the 29 events in this analysis, we calculate the ratio of the average peak amplitudes of the *S* waves (including the direct and secondary phases) recorded in the two subzones and call this quantity the *S* ratio; three aftershocks did not trigger at least two stations in one of the two subzones and are not used here. The *S* ratios range from 1.6 to 6.8, with a mean of 2.8 ± 1.1. A plot of the *S* ratios versus hypocentral distance, epicentral distance, depth, and magnitude of the 29 aftershocks shows that while there are no
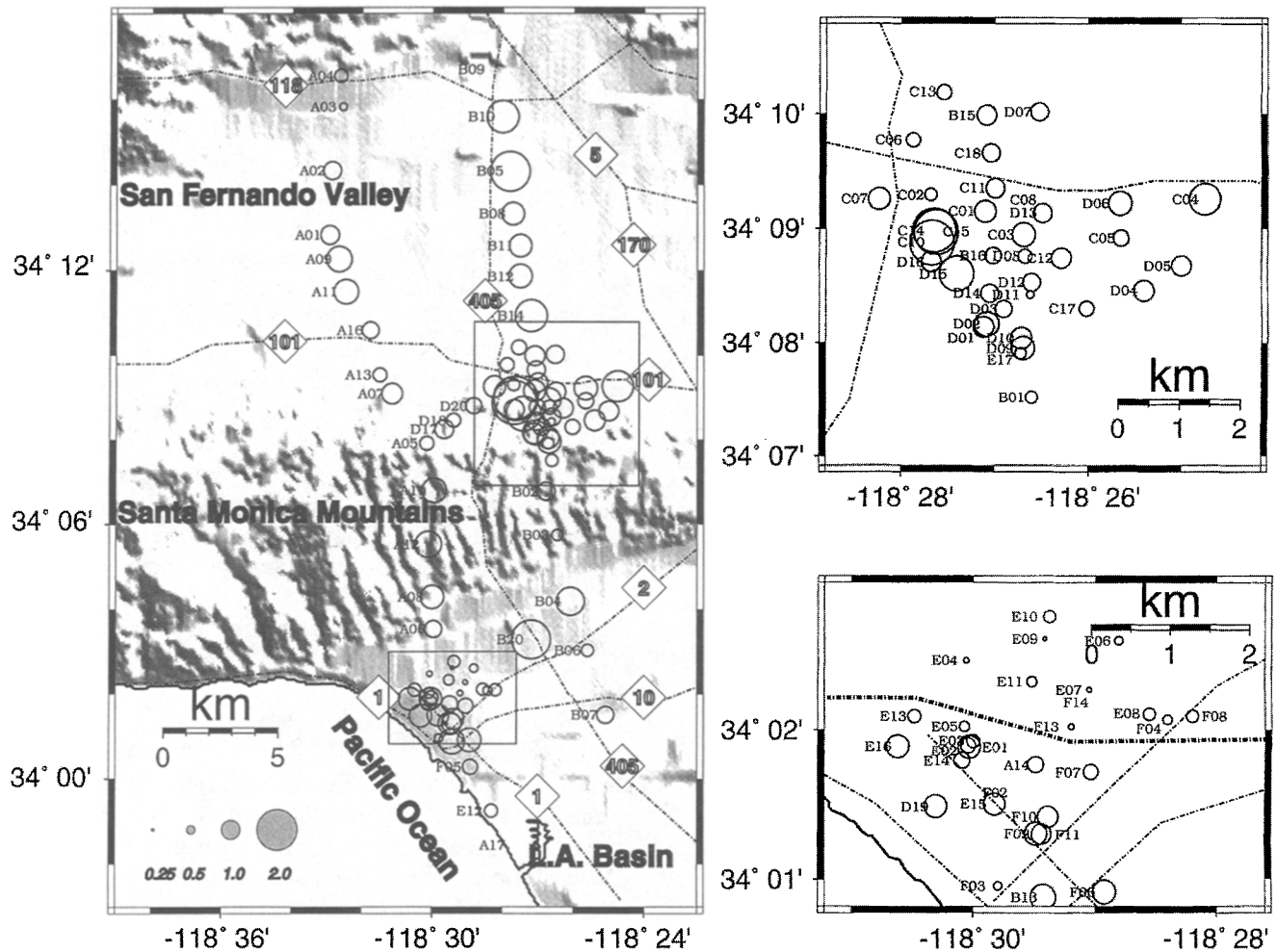
Figure 6.   Relative amplification factors of P waves at each station, averaged over 32
events. The size of the circle is proportional to amplitude (see legend). At the right are the
amplification factors for Sherman Oaks (upper) and Santa Monica (lower). The thick dashed
line in the Santa Monica inset is the boundary between heavily and slightly damaged zones.

significant correlations between the S ratios and focal dis-
tance or magnitude, the systematic variation of the ratio with
epicentral distance and depth is significant (Fig. 12). The
XCC's between the straight-line fitted and the observed val-
ues are 0.15, 0.32, 0.67, and 0.01 for focal distance, epicen-
tral distance, depth, and magnitude, respectively. The slopes
of these lines are -0.037/km, -0.073/km, 0.223/km, and
-0.042/m$_b$, respectively.

In Figure 13, we plot the epicenters of the aftershocks
as circles with size proportional to the S ratio; the darkness
of shading is proportional to the depth of the aftershock. We
find that events that have the greatest S ratios are mostly
relatively deep and concentrated on the southwestern side of
the aftershock zone; those events that have the smallest S
ratios are shallow and concentrated on the northeastern side
of the aftershock zone.

These observations suggest that the deeper the source

and the closer it is to Santa Monica, the larger the differential
damage will be. Therefore, the large differential damage
caused by the mainshock, whose hypocenter is 19-km deep
and which has an epicentral distance of about 21 km to Santa
Monica, appears to have resulted from a focusing of the
energy along a restricted set of azimuths and angles of in-
cidence from only portions of the fracture surface.

We tested a model in which focusing, as quantified by
the S ratio, decays as a function of the angle between the
direct ray from an aftershock and a critical ray, defined here
as the hypothetical ray with maximum focusing effect. Al-
though we do not know the exact geometry of the body that
causes focusing, amplitudes generally have an exponential
fall-off with distance from such a critical ray; we approxi-
mate this amplitude dependence with a second-order poly-
nomial at this level of accuracy. Using the 29 S ratios of
Table 2, a nonlinear Bayesian inversion (Jackson and Mat-
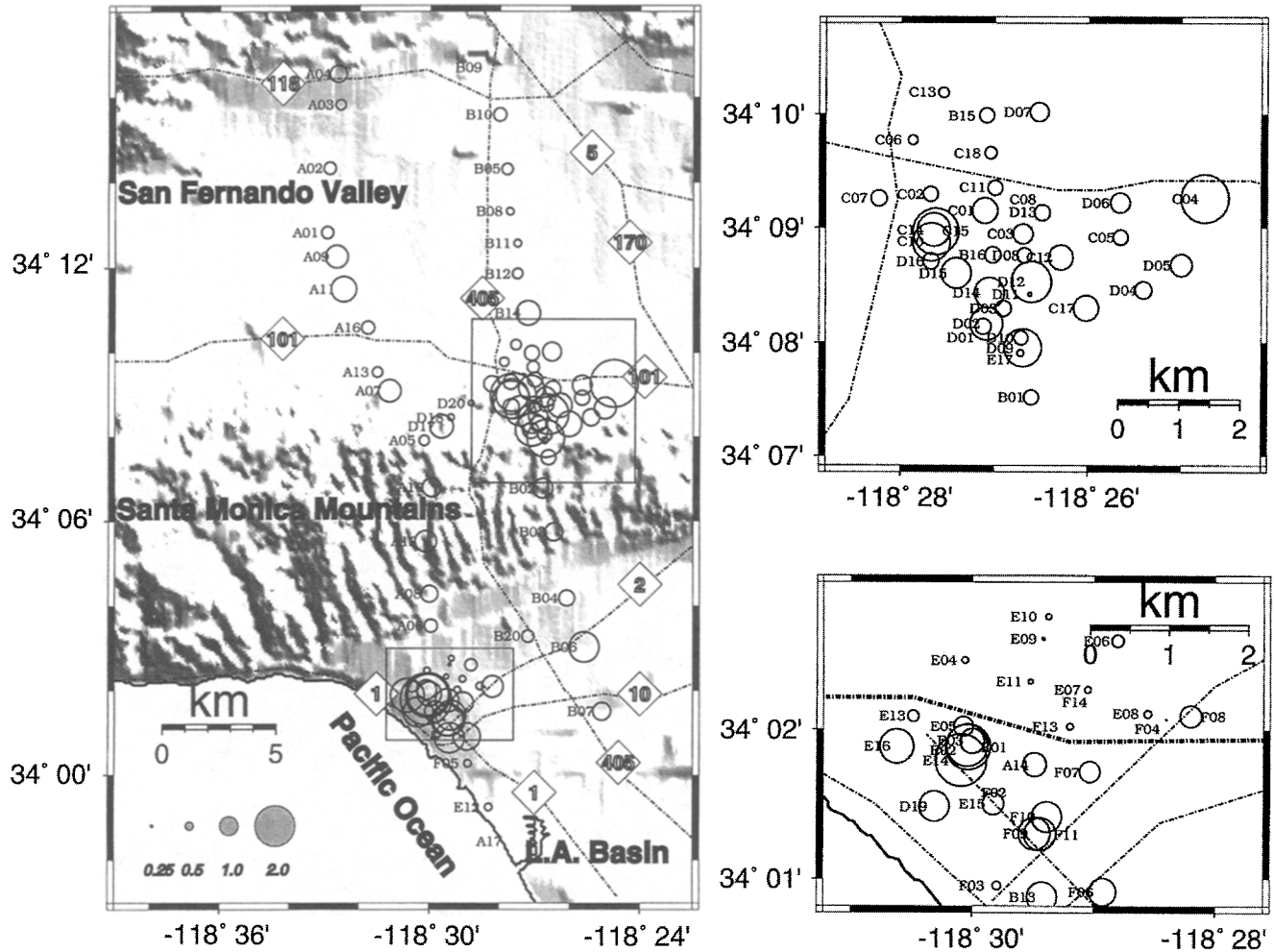
Figure 7. As in Figure 6 for *S* waves.

su'ura, 1985) was used to solve for the five parameters: a_1 and a_2, which are the azimuth and the angle of incidence of the critical ray, and a_3, a_4, and a_5, which are the coefficients of the second-order polynomial describing the decay of the *S* ratio. Station F07, which is approximately at the center of the Santa Monica array, was used as the reference station for the calculation of azimuths and angles of incidence.

Let the azimuth and angle of incidence of a direct ray from the *i*th aftershock measured in mid–Santa Monica be z_i and I_i. The angle between each direct ray and the critical ray is given by

$$\theta_i = \sqrt{(z_i - a_1)^2 + (I_i - a_2)^2}. \qquad (8)$$

If the *S* ratio of the *i*th aftershock is given by S_i, we fit

$$S_i = a_3 + a_4 \times \theta_i + a_5 \times \theta_i^2 \qquad (9)$$

by solving for the a_i. The fit of equation (9) to the *S*-ratio data is shown in Figure 12d. The XCC between the *S* ratios

and the polynomial is 0.90, which is quite significant. The angle of incidence of the critical ray is 53.5° measured from the vertical, and its azimuth is $-17.7°$ from the north. The resultant critical path is thus found to be close to that from the hypocenter of the mainshock, which has an angle of incidence of 48.0° and arrival azimuth of $-13.5°$. Therefore, there is a significant patch on the rupture surface of the mainshock that contributes rays that are near the critical ray. Thus, if our aftershock results are extended to the mainshock, the peak velocity of ground motion in mid–Santa Monica could have been more than eight times (Fig. 12d) larger during the mainshock than in the northern part, thereby possibly explaining the abnormally concentrated damage in mid–Santa Monica.

Seismic energy from aftershocks to the northeast of the Northridge fracture is not focused on the heavily damaged subzone (Fig. 13). It is therefore not surprising that the 1971 San Fernando earthquake, whose fracture surface was close to the northeast part of the Northridge aftershock zone, did not cause significant differential damage in this subzone.
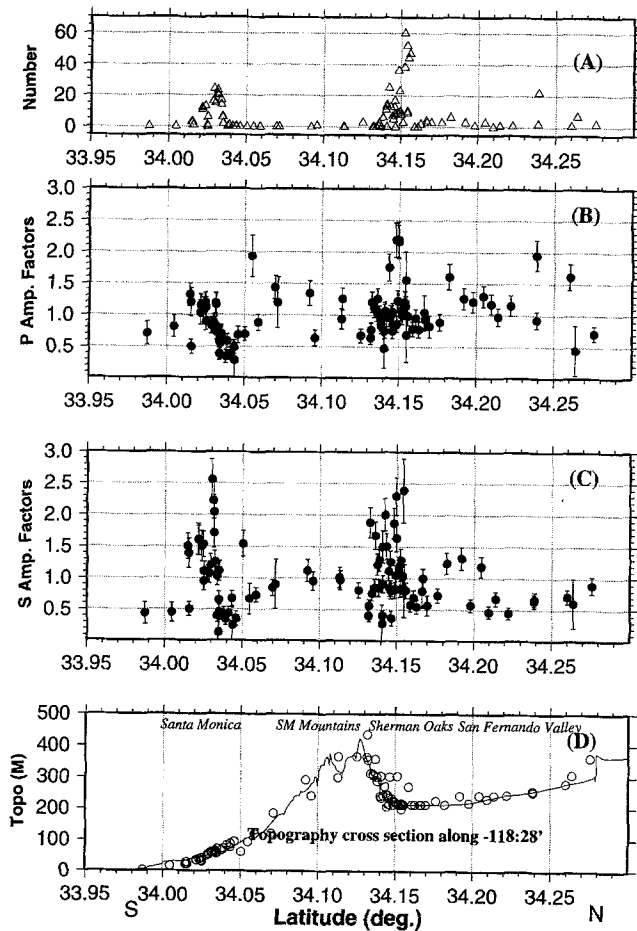
Figure 8.   (a) Cross sections of damage pattern, (b and c) P- and S-wave amplification factors, (d) topography and station elevations. Figure (a) is the number of red-tagged buildings within a rectangle of dimensions 2 by 0.5 km elongated in the E–W direction and entered at the station. the density of red-tagged structures in the central portion, between latitudes 34.05° and 34.12°, may be under-represented because of the low density of construction in the Santa Monica Mountains. Vertical bars in Figures (b) and (c) indicate the standard deviation of the mean. The solid line on Figure (d) is the elevation in meters along longitude −118°28', and the circles are the actual elevations of the stations.

Figure 9.   Normalized number of red-tagged buildings (dots) and normalized S- and P-wave amplification factors (diamonds) for (a and b) Santa Monica and (c and d) Sherman Oaks.

There is no clear variation of the S ratio with magnitude, implying that at least in the range of weak motions associated with the aftershocks, magnitude does not have a strong influence on amplification factors. Since both the heavily and slightly damaged areas are covered by Quaternary soil of similar type (Dibblee, 1991), nonlinear soil effects (Chin and Aki, 1991) probably did not play an important role in determining differential damage in Santa Monica from the mainshock.

Comparison with Strong-Motion Results.   A critical path for energy focused into mid–Santa Monica can explain the
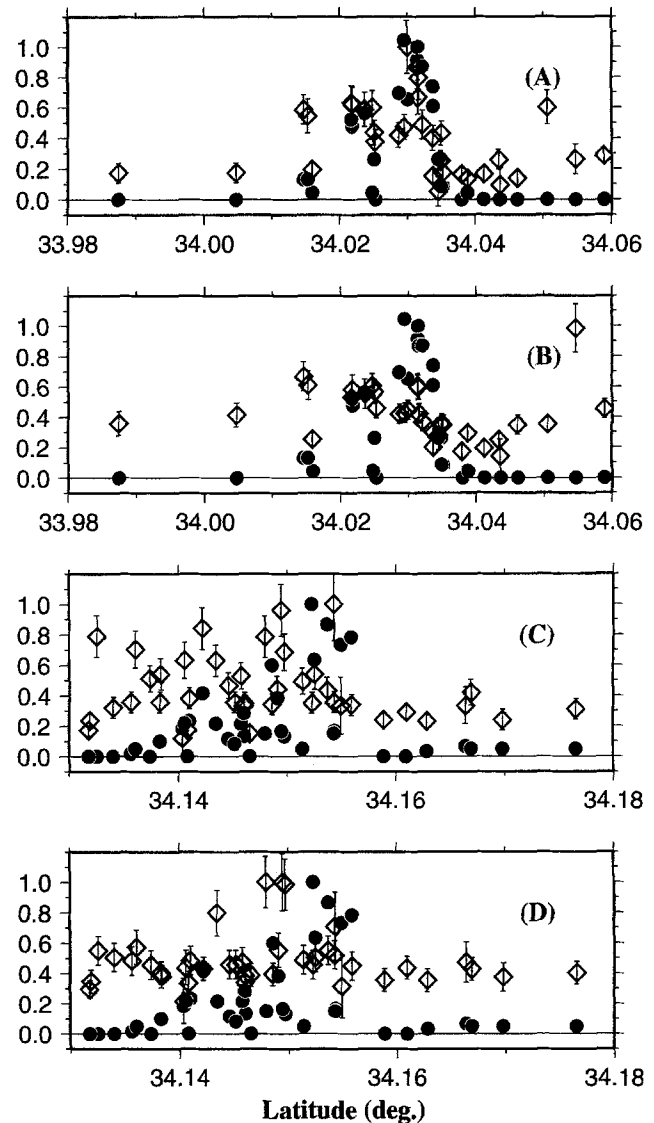
second large phase on the strong-motion record of the main event at Santa Monica City Hall. This phase has been attributed to a second subevent within the mainshock sequence that was located northwest of the epicenter (Wald and Heaton, 1994). Although it was seen on other strong-motion seismographs in Los Angeles, it had by far its largest amplitude in mid–Santa Monica.

Figure 14 displays 3-component strong-motion seismograms recorded at stations S MONICA (34.011°; −118.490°) and UCLAGRDS (34.068°; −118.439°) and their spectra. Station S MONICA is located about 0.4 km south of station B13, which is in the south-central part of the inset to Figure 7; UCLAGRDS is located about 0.4 km west of station B04. The ratio between the amplitude of the
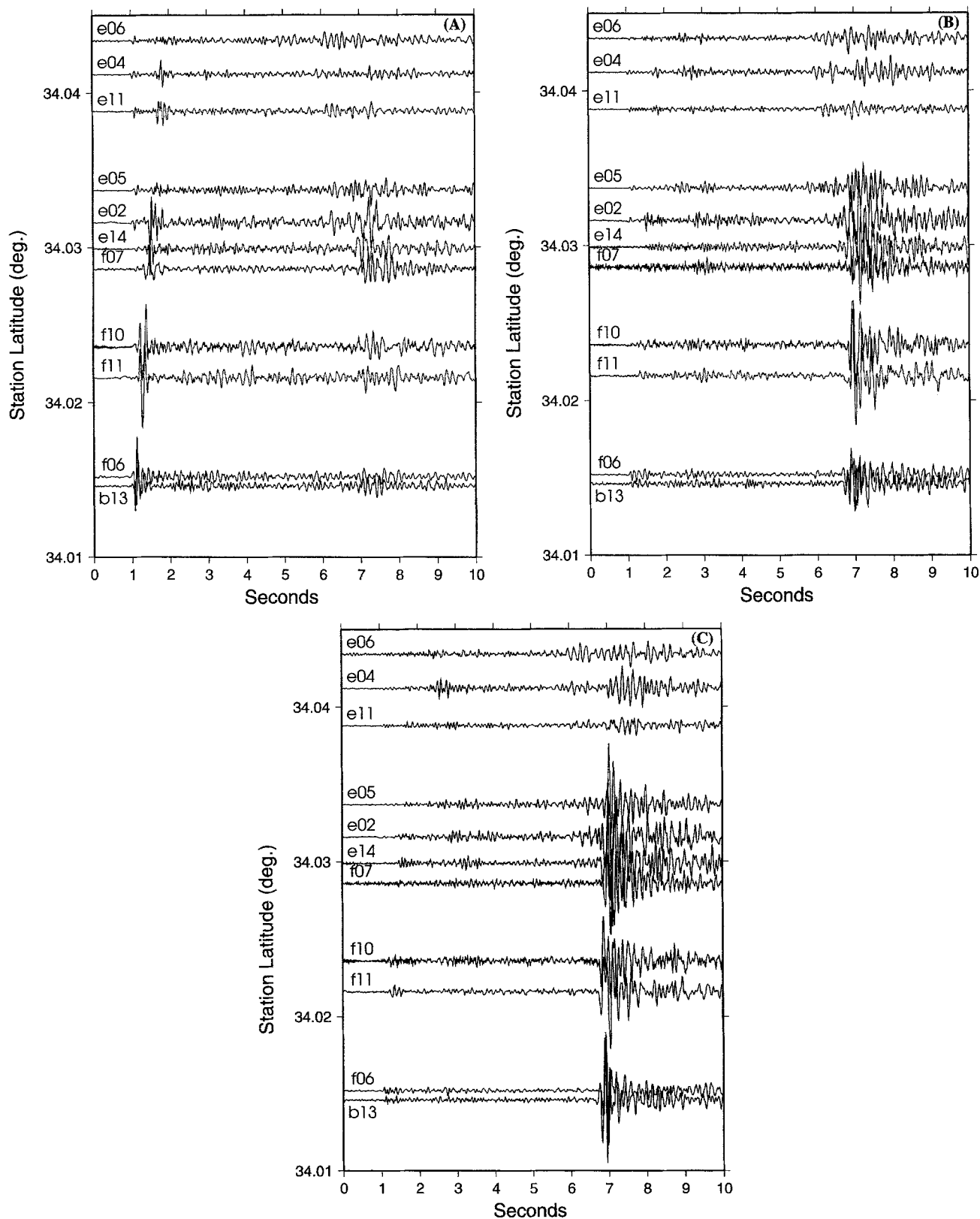
Figure 10.   Record section from event 1 showing the (a) vertical, (b) north–south, and (c) east–west components. Only the first 9 sec after the first arrival are shown. The traces are aligned with the first *P* arrivals at 1 sec and are plotted using the same scale.
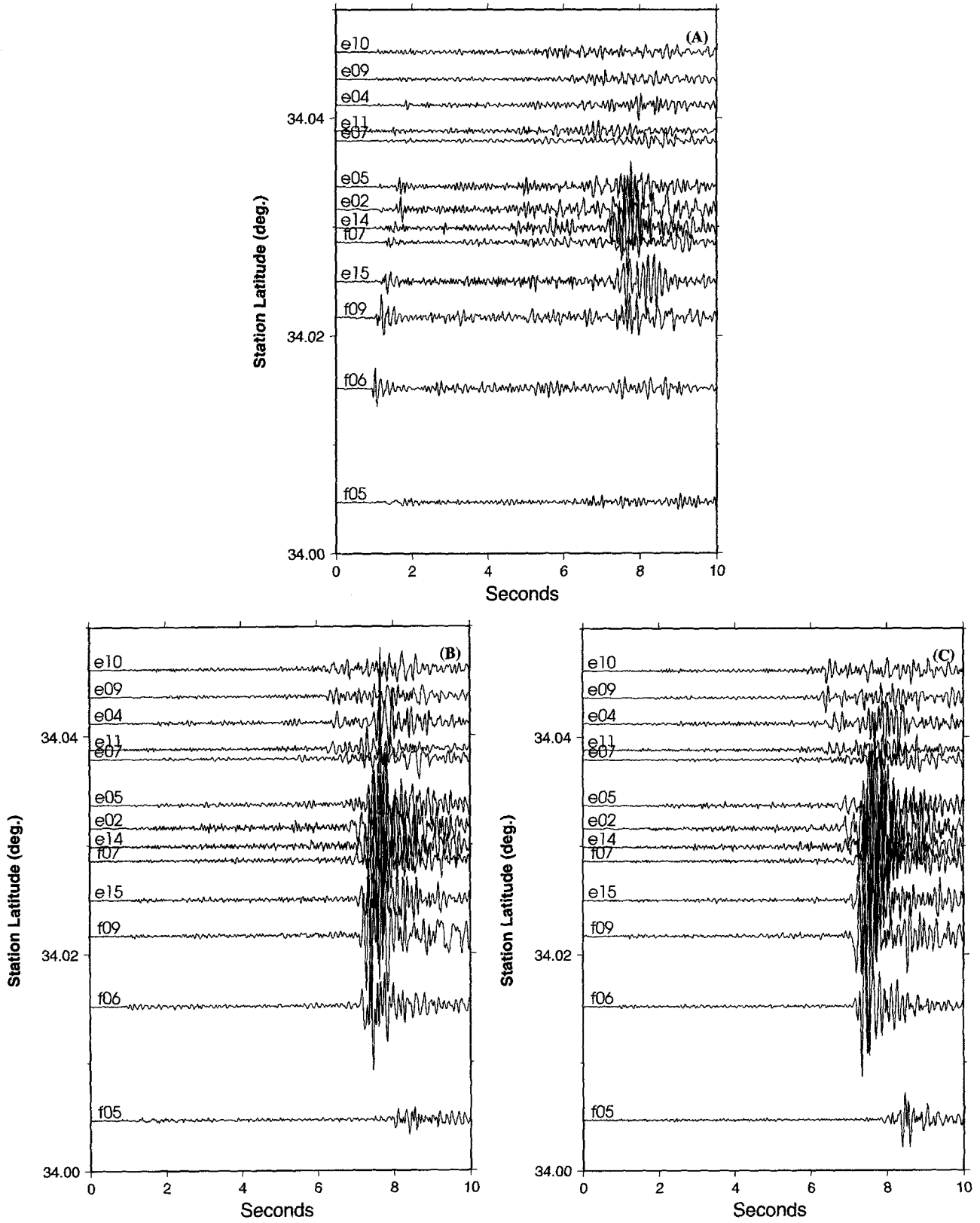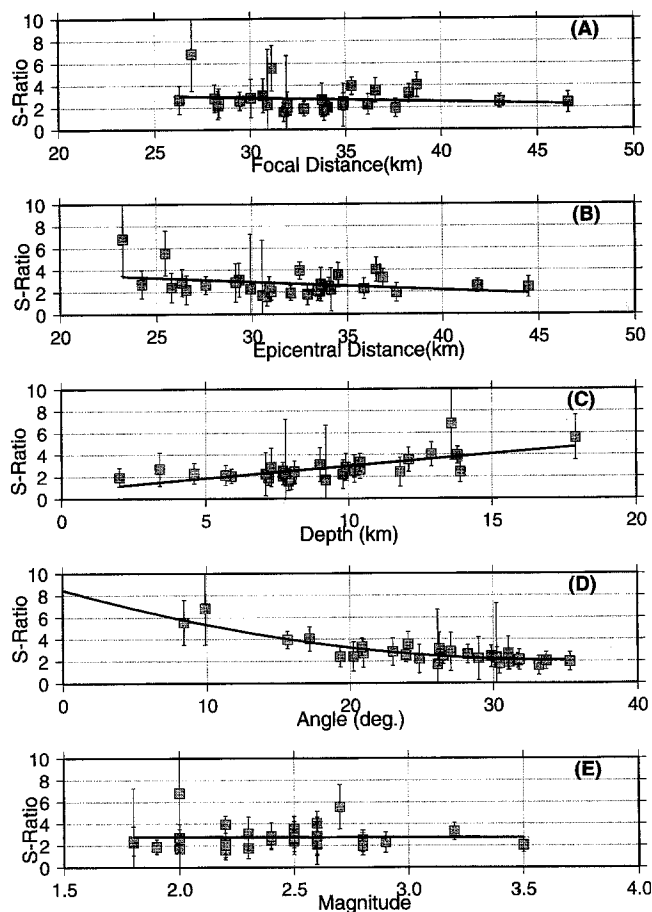
Figure 11. As in Figure 10 for event 4.

Figure 12.   *S* ratios between the heavily damaged and slightly damaged subzones of Santa Monical versus (a) focal distance, (b) epicentral distance, (c) depth, (d) differential angle, and (e) magnitude.

horizontal component of the second subevent phase that arrives at S MONICA at about 9 sec, on Figure 14, and at UCLAGRDS at about 8.5 sec is about 2. We interpret that this enhancement was due to the energy from the subevent traveling near the critical focusing path that we have found from the aftershocks.

Effects of Surface Geology.   Typically, peak ground velocities observed at soil sites can be about two to three times greater than at hard-rock sites (e.g., Barosch, 1969; Rogers *et al.,* 1984). Neither the damage nor our amplitude distributions can be simply explained by assuming that there are important site effects. For instance, stations on rock sites in the Santa Monica Mountains have similar or even higher amplitudes than stations in the San Fernando Valley and the Los Angeles Basin, except for the stations in the two heavily damaged zones. In Santa Monica, all the stations were located on Quaternary basin sediments (Wright, 1991; Dibblee, 1991; Hummon *et al.,* 1994), but the amplitudes vary considerably and can be more than eight times larger in mid–Santa Monica.

We therefore suggest that surface geology is not responsible for the enhanced damage. This view is corroborated by the damage pattern caused by the mainshock (Fig. 1). The damage in mid–Santa Monica was at the same level or even heavier than that in the San Fernando Valley, in spite of the fact that both are on Quaternary sediments and that the former is located at a larger distance from the epicenter.

Comparison with S–Coda Wave Amplification Factors.
Coda waves can be used to evaluate site effects. Coda waves are thought to consist of backscattered waves that arrive from all directions. This natural averaging process makes coda wave amplification factors a stable estimator of averaged site-response factors (e.g., Su and Aki, 1995; Kato *et al.,* 1995). Under usual circumstances, the amplification factors determined from coda waves and *S* waves agree with each other (e.g., Kato *et al.,* 1995).

In order to compare coda wave amplitudes with the direct wave amplitudes studied above, we measured the spatial variation of *S*-coda wave amplification factors on the horizontal components in two frequency bands and used the spectral ratio method described by Kato *et al.* (1995) to obtain coda amplitudes. The coda wave trains were extracted using a cosine-tapered window of length 4.096 sec (the number of points in the window is $4.096 \times 125 = 524$). The starting time of the window is twice the *S*-wave lapse time from the northernmost event to the southernmost station, which is about 13.5 sec. Thus, the window starts at 27 sec and ends at 31.096 sec after the origin time. We calculate spectral ratios in 2 octave frequency bands, 4 to 8 and 8 to 16 Hz, where the signal-to-noise ratio is highest.

The signals in the two coda windows were Fourier transformed separately for the two horizontal seismograms from the *j*th event at the *i*th station. The sum of the absolute amplitudes of the spectra was calculated over one of the frequency bands above to obtain the values of $A1_{ij}(f)$ and $A2_{ij}(f)$, where $A1$ is the amplitude for the N–S component and $A2$ is for the E–W component. A noise sample of 4.096 sec was taken prior to the origin time of the event from the two components and was also cosine-tapered, Fourier transformed, and summed to get $N1_{ij}(f)$ and $N2_{ij}(f)$. The pure horizontal coda amplitude in this frequency band is obtained using

$$R_{ij}(f) = A_{ij}(f) - N_{ij}(f), \qquad (10)$$

where $A_{ij}(f) = A1_{ij}(f) + A2_{ij}(f)$ and $N_{ij}(f) = N1_{ij}(f) + N2_{ij}(f)$.

The same procedure was performed for a base station to get reference values $A0_{ij}(f)$, $N0_{ij}(f)$, and $R0_{ij}(f)$. We selected the base station to be D10, which is located in the Santa Monica Mountains at which 32 aftershocks were recorded (Table 2).

The horizontal *S*-coda amplification factor relative to the base station is calculated using
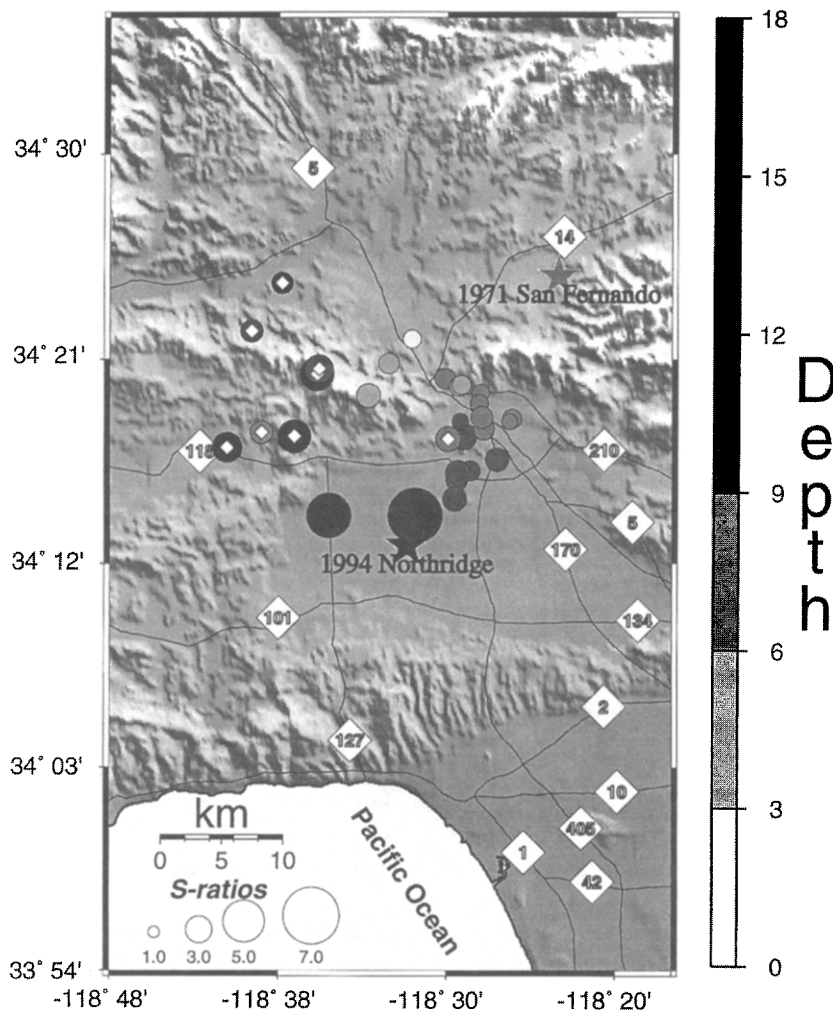
Figure 13. S ratios for Santa Monica at the corresponding epicenters, as well as the depth of the events. The size of the circles represents the relative S ratio. The shading gives the approximate depth of the events; the darkest events are deepest. Events with diamonds are those with observable secondary phases at stations in mid–Santa Monica. Location and darkness of the two stars show the hypocenters of the 1994 Northridge and 1971 San Fernando earthquakes.

$$C_{ij}(f) = \frac{R_{ij}(f)}{R0_{ij}(f)}. \tag{11}$$

To ensure a high signal-to-noise ratio, a seismogram is not used if $A_{ij}(f) < 3 \times N_{ij}(f)$, and none of the records from the event is used for the frequency band if $A0_{ij}(f) < 2 \times N0_{ij}(f)$. The final coda amplification factors are obtained by averaging all the measurements from available events. To make them comparable to S-wave amplification factors, the coda factors were normalized by the mean for each frequency band. Table 3 lists the resulting coda amplification factors and their standard deviations. The spatial variations and the cross sections are displayed in Figures 15 and 16, respectively.

From a comparison of the coda and S-wave amplification factors (Figs. 16 and 8) and the damage pattern caused by the mainshock (Fig. 1), we make the following observations:

1. In the heavily damaged mid–Santa Monica area, the averaged coda amplification factor is about 1.5 times that

in the slightly damaged northern part of the city. The ratio is about half of the value for S-wave amplification factors and one-fifth of the maximum S-wave ratio.

2. The coda amplification factors in the damage zones in Sherman Oaks are higher than surrounding areas but are about two-thirds of the value for the corresponding S-wave amplification factors (Fig. 8).

3. In Santa Monica, there is no significant dependence of coda amplification factors on source location.

Thus, site effects may have contributed to the damage that occurred in Santa Monica and Sherman Oaks, but focusing effects identified in Santa Monica were probably five times more severe. Further analysis is required to separate these effects for Sherman Oaks.

A Preliminary Structural Model for Santa Monica. We do not have enough information from structural geology to be able to pinpoint the features of the structures that cause focusing. However, our results suggest that a contact between high-velocity material underlying the Santa Monica Moun-
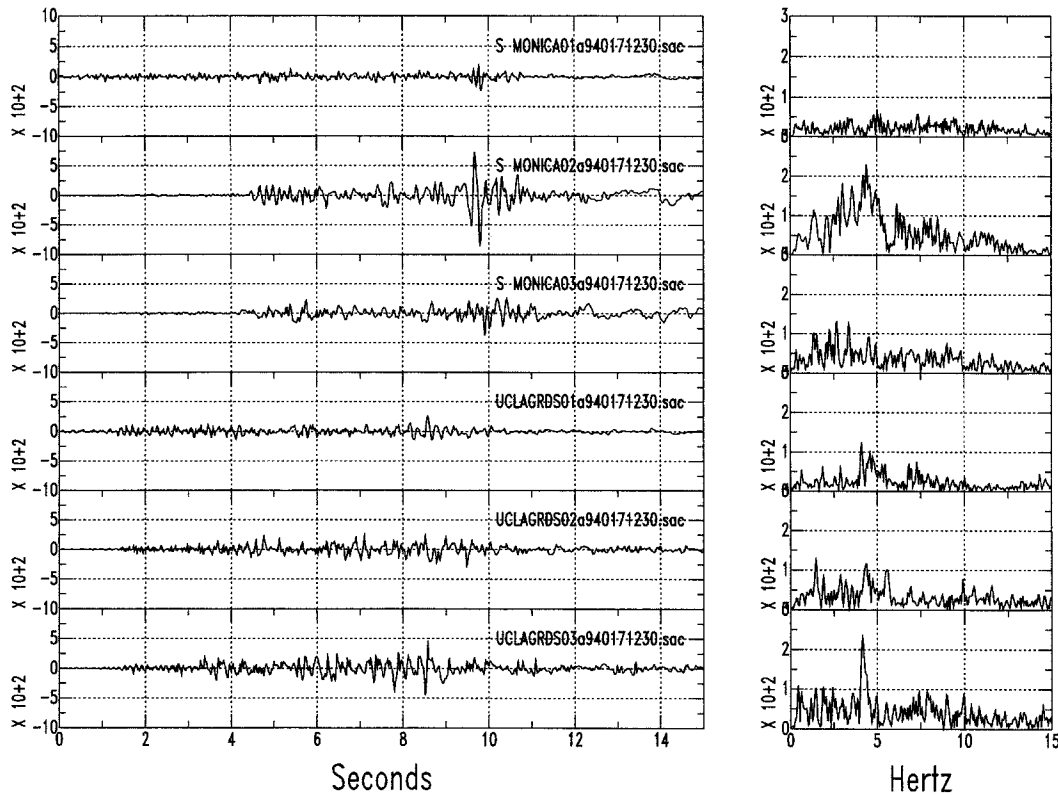
Figure 14.   Three-component strong-motion acceleration seismograms recorded at stations S_MONICA (34.011°, −118.490°) and UCLAGRDS (34.068°, −118.439°) and their spectra. Station S_MONICA is located about 0.4 km south of station B13, which is in the south-central part of the Santa Monica inset (see Fig. 7), and UCLAGRDS is located at about 0.4 km west of station B04. The top three seismograms are the 3-component records from S MONICA, and the lower three are from UCLAGRDS.

tains and low velocities of the Los Angeles Basin is warped to form a 3D lens that focuses waves arriving from the north on sites in mid–Santa Monica (Fig. 17). The northern boundary of the basin lens in Figure 17 may be the Santa Monica fault that dips northward at about 50° in this area, with an offset of more than 2 km to the basement in the basin (Wright, 1991). The observations in Santa Monica can be explained by this model as follows:

1. The first phase corresponds to the upper ray of the diagram; it is a direct ray that is refracted by the fault. The second and larger amplitude phase corresponds to the lower rays that represent focusing of seismic energy by a low-velocity lens created by a sub-basin. For events with rays whose angles of incidence are steeper than the dip of the fault, negligible energy is refracted by the fault and nearly all the energy received by the stations in mid–Santa Monica was focused by the lens. This may explain the absence of secondary phases from events 6 and 10, which are deep and close to Santa Monica and have the steepest angles of incidence (Fig. 13).

2. Since the first phase arrives at a larger angle of incidence than the secondary phase, its apparent velocity is smaller than the second and larger phase (Figs. 10 and 11).

3. The focusing of the second phase explains its large amplitudes and its variability across the damage zone. The earlier phase is a simple refraction that is expected to have relatively uniform amplitudes at all stations, as observed.

4. Focusing in mid–Santa Monica, as indicated by the *S* ratios, occurs only for a bundle of rays from a restricted range of angles of incidence, spanning about 20° around the ray and which are presumed to pass through the vertex of the lens. The other rays are either not focused or the focal point is offshore.

5. The reason why the difference of *S*-wave amplification factors between the central and northern parts of Santa Monica is significantly larger than the coda amplification factors is that *S*-wave energy is focused on the stations through the lens, while coda wave rays, being omnidirectional, are not.

We are currently refining this model by incorporating what is known about deep geologic structure in the region.
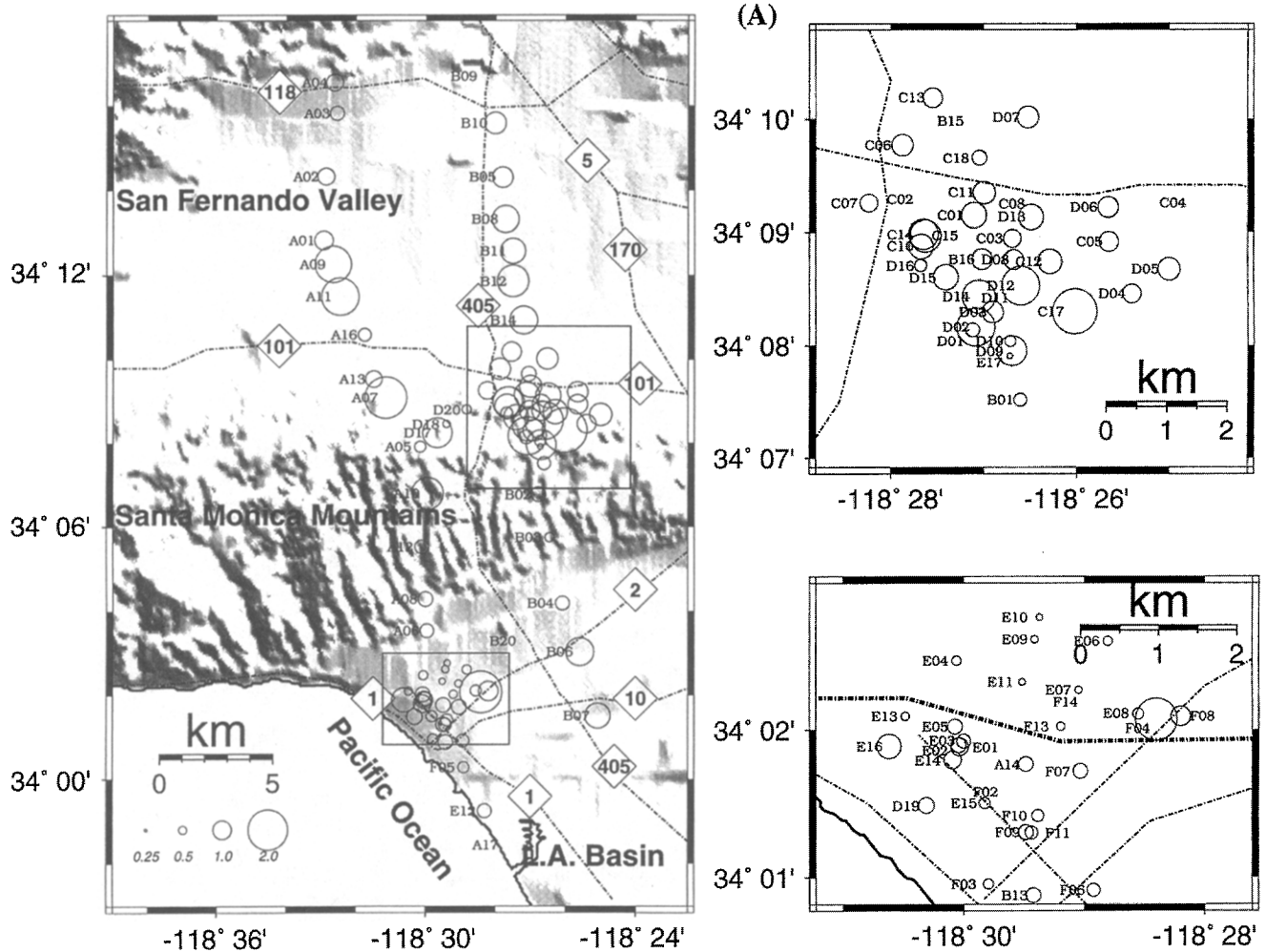
Figure 15(a).   Relative coda amplification factors for frequency bands (a) 4 to 8 Hz.

Conclusions

1. There were 98 Reftek stations deployed during a 3-week period to record Northridge aftershocks. About 7 gigabytes of data were collected to investigate effects of structure on seismic amplitudes.

2. Preliminary results show that both P- and S-wave peak amplitudes from 32 aftershocks are well correlated with the damage pattern caused by the mainshock. Two anomalously highly damaged areas, Sherman Oaks and mid–Santa Monica, display two to three times higher amplification than areas surrounding them.

3. A double phase was observed in Santa Monica from a number of events. The amplitudes of the later-arriving P and S phases are about 10 times greater than those of the first arriving P and S waves in the heavily damaged zone. These large amplitude signals decrease rapidly in the slightly damaged zones.

4. In the case of Santa Monica, the critical path for focusing the incident energy lies to the west of the mainshock. These results suggest that a slight change in the location of a mainshock from the Northridge fracture surface would have created significant changes in the damage pattern in Santa Monica.

5. We propose a preliminary model to explain the observations in Santa Monica that involves a deep convex structure that focuses rays selectively in mid–Santa Monica. The northern boundary to this structure may be the Santa Monica fault.

6. Site effects are about five times smaller in mid–Santa Monica than the focusing effects due to the deeper lens.
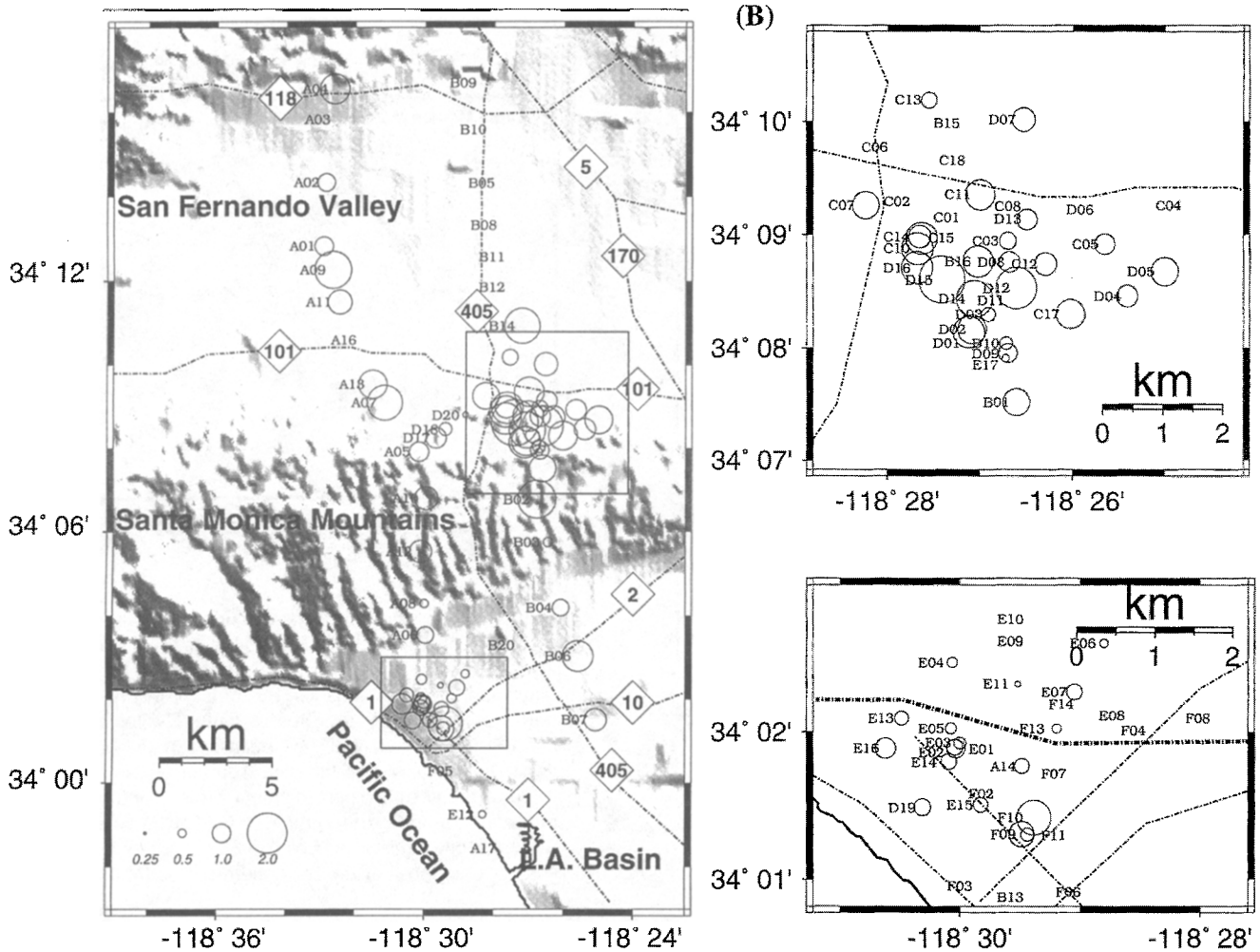
Acknowledgments

Figure 15(b). Eight to 16 Hz at each station. The size of each circle is proportional to the amplification factor (see legend). At the right are the amplification factors for Sherman Oaks (upper) and Santa Monica (lower). The thick dashed line in the Santa Monica inset is the boundary between heavily and slightly damaged zones.

References

Aki, K. and P. G. Richards (1980). *Quantitative Seismology: Theory and Methods*, W. H. Freeman, San Francisco, California.

Aki, K. (1993). Local site effects on weak and strong ground motion, *Tectonophysics* **218**, 93–111.

Barosch, P. J. (1969). Use of seismic intensity data to predict the effects of earthquakes and underground nuclear explosions in various geologic settings, *U.S. Geol. Surv. Bull.* **1279**, 93 pp.

Chin, B. and K. Aki (1991). Simultaneous study of the source, path, and site effects on strong ground motion during the 1989 Loma Prieta earthquake: a preliminary result on pervasive nonlinear site effects, *Bull. Seism. Soc. Am.* **81**, 1859–1884.

Dibblee, T. W. Jr. (1991). Geological map of the Beverly Hills and Van Nuys (South 1/2) quadrangles, Los Angeles county, California, Dibblee Geological Foundation, Santa Barbara, California.

Hummon, C., C. L. Schneider, R. S. Yeats, J. Dolan, K. E. Sieh, and G. J. Huftile (1994). Wilshire fault: earthquake in Hollywood? *Geology* **22**, 291–294.

Jackson, D. D. and M. Matsu'ura (1985). A Bayesian approach to nonlinear inversion, *J. Geophys. Res.* **90**, 581–591.

Jones, L. and E. Hauksson (1988). The Whittier Narrows, California earthquake of October 1, 1987; Seismology, *Earthquake Spectra* **4**, 43–54.

Kato, K., K. Aki, and M. Takemura (1995). Site amplification from coda waves: validation and application to S-wave site response, *Bull. Seism. Soc. Am.* **85**, 667–477.

Kawase, K. and K. Aki (1990). Topography effect at the critical SV-wave incidence: possible explanation for damage pattern by the Whittier
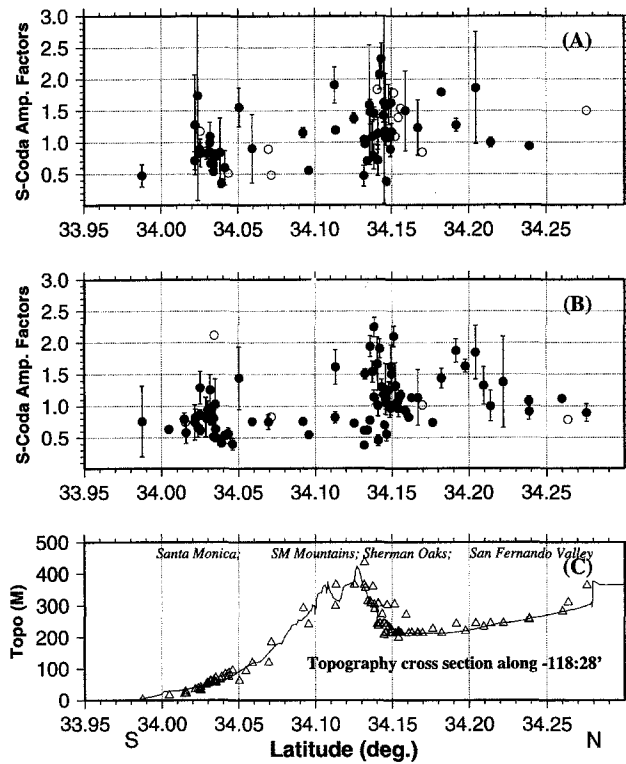
Figure 16. Cross-section of coda wave amplification factors for (a) 8 to 16 Hz and (b) 4 to 8 Hz (b) and (c) station elevations. Open circles are stations with only one measurement, and filled circles are those with more than one measurement.
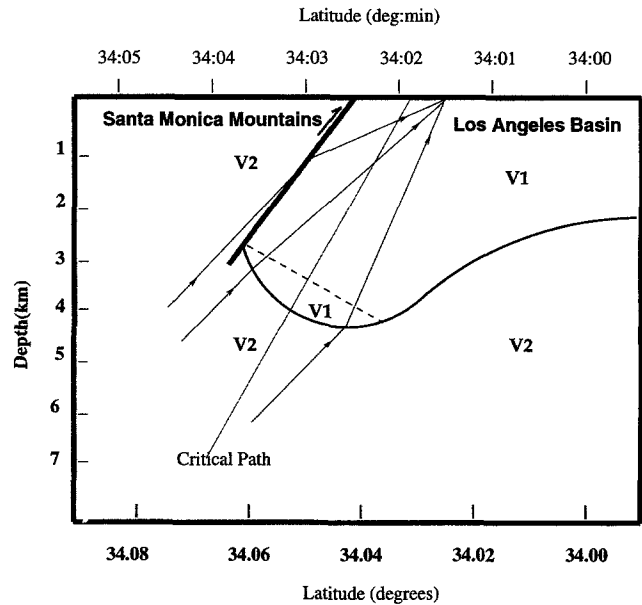

Figure 17. Schematic cross section to explain observations of amplitudes in Santa Monica. The boundary of separation between the Santa Monica Mountains and the Los Angeles Basin is probably the northward-dipping Santa Monica fault. The location and dip of the fault and the dimension of the basin basement are based on the data from an oil well located at the northern part of Santa Monica and geophysical exploration (Wright, 1991). The P- and S-wave velocities inside the Los Angeles Basin (V1) are smaller than those of the surrounding areas (V2).

Narrows, California, earthquake of October 1, 1987, *Bull. Seism. Soc. Am.* **80**, 1–22.

Marshall, G. A. and R. S. Stein (1994). Severely damaged blocks or buildings judged unsafe for occupation by FEMA, State OES, and City & County of LA inspectors, *U.S. Geol. Surv. Open-File Rept. 94-442*, July.

Rogers, A. M., R. D. Borcherdt, P. A. Covington, and D. M. Perkins (1984). A comparative ground response study near Los Angeles using recordings of Nevada nuclear tests and the 1971 San Fernando earthquake, *Bull. Seism. Soc. Am.* **74**, 1925–1949.

Su, F. and K. Aki (1995). Site amplification factors in Central and Southern California determined from coda waves, *Bull. Seism. Soc. Am.* **85**, 452–466.

USGS (U.S. Geological Survey) and SCEC (Southern California Earthquake Center) (1994). The magnitude 6.7 Northridge, California, earthquake of 17 January 1994, *Science* **266**, 389–397.

Wald, D. J. and T. H. Heaton (1994). A dislocation source model of the

1994 Northridge, California, earthquake determined from strong ground motions, *U.S. Geol. Surv. Open-File Rept. 94-278*, 53 pp.

Wright, T. L. (1991). Structural geology and tectonic evolution of the Los Angeles basin, California, in *Active Margin Basins: American Association of Petroleum Geologists Memoir 52*, K. E. Biddle (Editor), 35–134.

Department of Earth and Space Sciences
University of California
Los Angeles, California 90095
(S.G., H.L., P.M.D.)

Department of Physics and Institute of Geophysics and Planetary Physics
University of California
Los Angeles, California 90095
(L.K.)

Table 3
S-coda Wave Amplification Factors

Station Name	Coordinates		Amp. Factor (4–8 Hz)			Amp. Factor (8–16 Hz)		
	Latitude (°N)	Longitude (°E)	Mean	Std	No. Events	Mean	Std	No. Events
A01	34.213924	−118.548698	1.01	0.24	6	1.00	0.08	3
A02	34.238934	−118.547394	0.91	0.13	11	0.94	0.04	4
A03	34.263672	−118.542450	0.78	—	1	—	—	0
A04	34.275669	−118.543457	0.89	0.14	7	1.50	—	1
A05	34.131889	−118.502686	0.61	0.04	26	1.04	0.04	24
A06	34.058853	−118.499374	0.75	0.05	17	0.90	0.54	4
A07	34.151409	−118.519020	2.10	0.16	9	1.78	—	1
A08	34.071354	−118.500000	0.83	—	1	0.48	—	1
A09	34.204437	−118.544273	1.84	0.43	8	1.86	0.88	2
A10	34.113281	−118.499084	1.62	0.27	12	1.19	0.06	8
A11	34.191669	−118.540886	1.87	0.18	9	1.27	0.10	5
A12	34.092056	−118.501823	0.76	0.06	12	1.15	0.08	7
A13	34.158855	−118.524872	0.92	0.08	11	1.50	0.63	6
A14	34.029427	−118.491402	0.81	0.07	16	0.83	0.10	7
A16	34.176548	−118.529167	0.74	0.05	5	—	—	0
B01	34.125263	−118.443398	0.72	0.06	17	1.38	0.08	13
B02	34.112915	−118.446220	0.82	0.09	6	1.91	0.29	4
B03	34.095833	−118.440758	0.54	0.06	15	0.56	0.06	9
B04	34.069660	−118.434639	0.75	0.12	5	0.89	—	1
B05	34.238670	−118.463280	1.08	0.08	5	—	—	0
B06	34.050522	−118.426300	1.44	0.49	7	1.56	0.31	6
B07	34.025185	−118.417915	1.29	0.26	4	1.18	—	1
B08	34.222137	−118.461845	1.38	0.72	3	—	—	0
B10	34.259895	−118.466927	1.12	0.04	2	—	—	0
B11	34.209637	−118.458328	1.32	0.30	4	—	—	0
B12	34.197735	−118.458328	1.63	0.10	5	—	—	0
B13	34.014610	−118.490417	0.79	0.10	3	—	—	0
B14	34.182293	−118.453384	1.44	0.16	5	1.79	0.00	2
B15	34.166416	−118.451508	—	—	0	—	—	0
B16	34.146069	−118.450325	1.10	0.11	11	1.57	0.52	7
B20	34.054688	−118.453125	—	—	0	—	—	0
C01	34.152493	−118.451706	1.32	—	1	—	—	0
C02	34.154907	−118.461411	—	—	0	—	—	0
C03	34.149090	−118.444923	0.96	0.10	7	0.90	0.12	3
C04	34.154320	−118.412445	—	—	0	—	—	0
C05	34.148598	−118.427498	1.02	0.20	5	1.08	0.03	3
C06	34.162838	−118.464607	1.13	0.03	2	—	—	0
C07	34.154297	−118.470573	0.96	0.13	4	1.39	—	1
C10	34.147968	−118.461243	1.25	0.13	4	1.60	0.32	7
C11	34.155861	−118.449867	1.17	0.08	2	1.54	—	1
C12	34.145744	−118.438126	1.27	0.40	9	1.17	0.14	6
C13	34.169792	−118.459114	1.01	—	1	0.84	—	1
C14	34.149746	−118.460838	1.50	0.15	6	1.17	0.13	4
C15	34.149471	−118.460495	1.63	0.34	2	1.63	0.23	5
C17	34.138355	−118.433693	2.24	0.15	18	1.46	0.10	16
C18	34.160938	−118.450775	0.82	0.04	4	—	—	0
D01	34.135647	−118.451981	0.77	0.05	10	1.59	0.95	3
D02	34.136059	−118.451416	1.94	0.16	17	1.48	0.20	12
D03	34.138283	−118.448410	1.14	0.11	17	0.77	0.20	11
D04	34.140984	−118.423386	1.01	0.17	14	1.14	0.25	8
D05	34.144588	−118.416656	1.17	0.12	12	1.43	0.11	7
D06	34.153667	−118.427567	1.08	0.12	5	—	—	0
D07	34.166927	−118.442055	1.13	0.44	5	1.23	0.44	5
D08	34.146019	−118.444664	1.04	0.10	8	1.07	0.12	4
D09	34.132534	−118.444878	1.50	0.08	17	0.97	0.05	13
D10	34.133999	−118.445267	0.62	0.00	23	0.70	0.00	19
D11	34.140366	−118.443619	—	—	0	—	—	0
D12	34.142200	−118.443428	1.91	0.15	19	2.07	0.23	12
D13	34.152264	−118.441460	1.31	0.37	5	1.09	—	1

Table 3
Continued

Station Name	Coordinates		Amp. Factor (4–8 Hz)			Amp. Factor (8–16 Hz)		
	Latitude (°N)	Longitude (°E)	Mean	Std	No. Events	Mean	Std	No. Events
D14	34.140572	−118.450905	1.66	0.42	2	1.83	—	1
D15	34.143444	−118.456841	1.30	0.12	13	2.32	0.25	10
D16	34.145138	−118.461327	0.70	0.04	3	1.62	1.60	2
D17	34.137371	−118.494400	1.54	0.17	15	1.09	0.24	8
D18	34.140820	−118.489838	0.45	0.08	22	0.71	0.24	15
D19	34.024738	−118.505211	0.86	0.08	11	0.89	0.10	8
D20	34.146542	−118.480446	0.56	0.11	5	0.38	0.05	4
E01	34.031418	−118.500587	0.92	0.10	14	0.99	0.17	11
E02	34.031605	−118.500717	0.79	0.08	9	0.84	0.20	6
E03	34.032093	−118.499985	0.78	0.09	15	0.66	0.11	10
E04	34.041210	−118.501053	0.53	0.06	11	0.60	0.27	4
E05	34.033703	−118.501236	0.80	0.09	19	0.65	0.09	11
E06	34.043381	−118.480064	0.56	0.09	8	0.51	—	1
E07	34.037910	−118.484177	0.47	0.06	7	0.84	0.55	3
E08	34.035156	−118.475914	0.63	0.19	3	—	—	0
E09	34.043594	−118.490288	0.46	—	1	—	—	0
E10	34.046093	−118.489578	0.40	0.10	5	—	—	0
E11	34.038803	−118.492004	0.41	0.04	10	0.36	0.07	6
E12	33.987370	−118.471619	0.76	0.56	3	0.48	0.17	2
E13	34.034897	−118.508072	0.50	0.07	8	0.77	0.11	6
E14	34.029949	−118.501564	0.94	0.15	17	0.83	0.10	10
E15	34.025002	−118.497131	0.62	0.07	12	0.83	0.22	7
E16	34.031467	−118.510361	1.25	0.24	8	1.09	0.22	6
E17	34.131767	−118.445312	0.38	0.04	16	0.47	0.16	10
F03	34.015884	−118.496613	0.58	0.17	3	—	—	0
F04	34.034504	−118.473434	2.12	—	1	—	—	0
F05	34.004688	−118.481773	0.63	0.04	4	—	—	0
F06	34.015224	−118.482063	0.74	—	1	—	—	0
F07	34.028645	−118.483849	0.82	0.31	6	—	—	0
F08	34.034908	−118.469986	1.03	0.40	7	—	—	0
F09	34.021729	−118.491440	0.81	0.14	4	1.28	0.79	4
F10	34.023560	−118.489738	0.66	0.16	3	1.74	1.65	2
F11	34.021648	−118.490639	0.74	0.28	3	0.71	0.14	2
F13	34.033722	−118.486588	0.51	0.06	8	0.54	0.06	2